Geophys. J. Int. (2004) **159,** 1057–1076 doi: 10.1111/j.1365-246X.2004.02462.x

Upper mantle *S*-wave speed heterogeneity and anisotropy beneath the North Atlantic from regional surface wave tomography: the Iceland and Azores plumes

S. Pilidou,[1] K. Priestley,[1] Ó. Gudmundsson[2] and E. Debayle[3]

[1] *Bullard Laboratories, University of Cambridge, Cambridge, UK. E-mail: pilidou@esc.cam.ac.uk*
[2] *Danish Lithosphere Centre, Copenhagen, Denmark*
[3] *Ecole et Observatiore des Sciences de la Terre, Université Louis Pasteur, Strasbourg, France*

Accepted 2004 August 23. Received 2004 August 23; in original form 2003 October 15

SUMMARY

We present a high-resolution S_v-wave velocity and azimuthal anisotropy model for the upper mantle beneath the North Atlantic and surrounding region derived from the analysis of over 3000 fundamental and higher mode Rayleigh waveforms. Much of the data set comes from global and national digital seismic networks, but to improve the path coverage we have also deployed a number of instruments at coastal sites in northwest Europe, Iceland and eastern Greenland. The dense path coverage, wide azimuthal distribution, substantial higher mode content and the relatively short path-lengths in the data set have enabled us to build an upper-mantle model for the region with a horizontal resolution of a few hundred kilometres extending to 400 km depth. Three major hotspots, Iceland, Azores and Eifel, exist within the region of the model and slow upper-mantle velocities are associated with each of these areas. The best depth resolution in our model occurs in NW Europe and in this area low S_v velocities in the vicinity of the Eifel hotspot extend to approximately 400 km depth. Major negative velocity anomalies exist in the North Atlantic upper mantle beneath both Iceland and the Azores hotspots. Both anomalies are, above 200 km depth, 5–7 per cent slow with respect to PREM and are elongated along the Mid-Atlantic ridge. Low velocities extend to the south of Iceland beneath the Reykjanes ridge where other geophysical and geochemical observations have indicated the presence of hot plume material. A similar but somewhat weaker feature exists beneath the Kolbeinsey ridge north of Iceland, where there is also supporting evidence for the presence of hot plume material. This observation might also be associated with a plume beneath Jan Mayen. The low-velocity structure beneath the Azores hotspot is also elongated along the Mid-Atlantic ridge. The fast propagation direction of horizontally propagating S_v waves in the Atlantic south of Iceland correlates well with the east–west ridge-spreading direction at all depths and changes to a direction close to NS in the vicinity of Iceland.

Key words: azimuthal anisotropy, Azores, Eifel, Iceland, mantle plumes, surface wave tomography.

1 INTRODUCTION

The two major tectonic features of the North Atlantic ocean are the Mid-Atlantic ridge and the oceanic plateau surrounding Iceland (Fig. 1). The volcanic edifice on which Iceland sits results from enhanced melting as a result of the interaction of the Mid-Atlantic ridge and the Iceland plume (McKenzie 1984; Sleep 1990). While the crustal structure of Iceland has been intensely studied with a variety of geophysical methods (e.g. Bjarnason *et al.* 1993; Staples *et al.* 1997; Darbyshire *et al.* 2000a,b; Allen *et al.* 2002b), the width and depth extent of the plume core in the mantle beneath Iceland is controversial (e.g., Wolfe *et al.* 1997; Bijwaard & Spakman 1999; Keller *et al.* 2000; Foulger *et al.* 2001) and very little is known about the extent of the plume head in the upper mantle beneath the surrounding North Atlantic.

Early global tomographic studies produced images with too low resolution to resolve features possibly associated with hotspots in the North Atlantic. However, recent global models employing body wave data (e.g. Ritsema *et al.* 1999) clearly show low-velocity features in the uppermost mantle beneath the Iceland and Azores hotspots. Teleseismic body wave traveltime tomography has been used to argue for the existence beneath Iceland of both a continuous plume through the whole mantle (Bijwaard & Spakman 1999) and a plume confined to the upper mantle (Foulger *et al.* 2001). Bijwaard

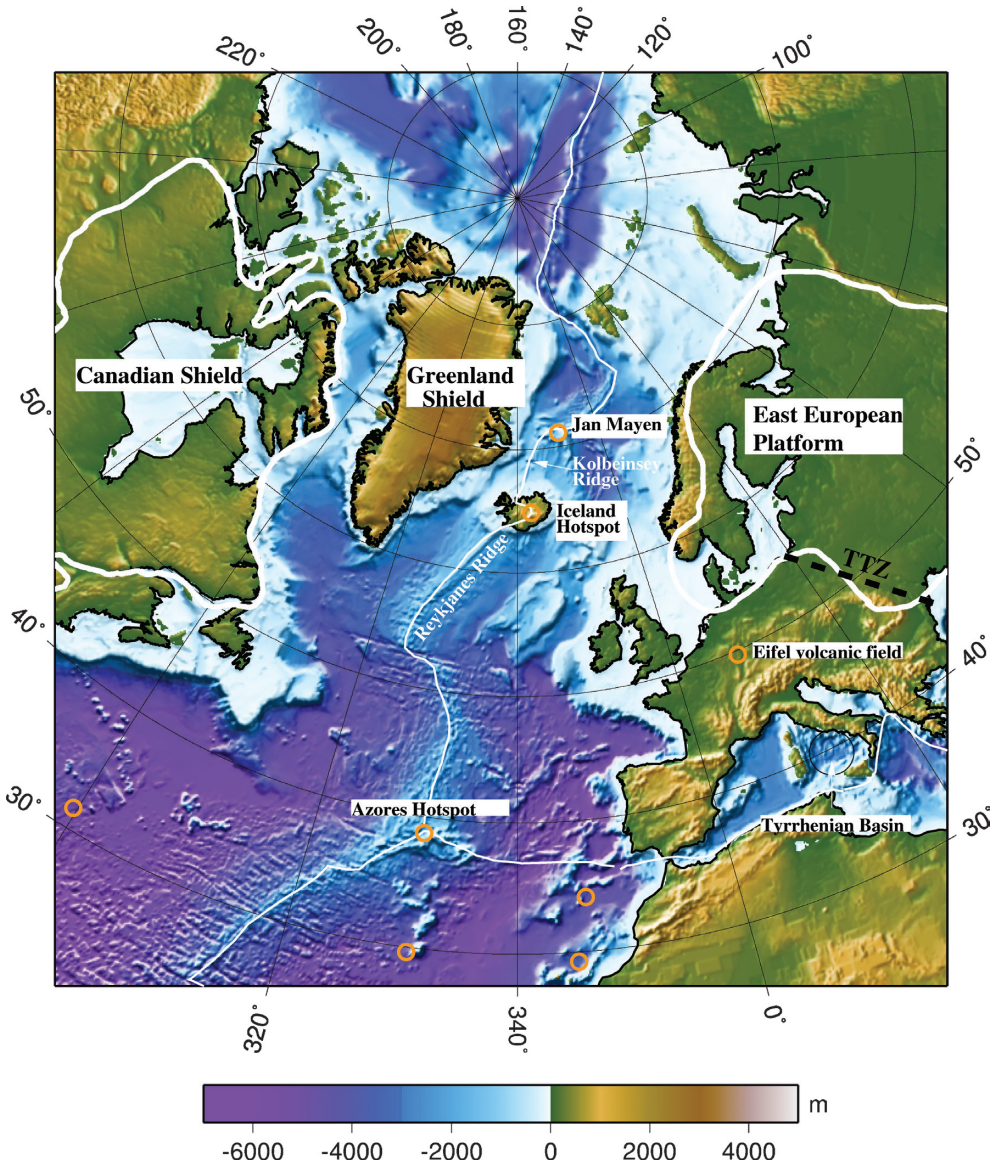

Figure 1. Topography and bathymetry of the North Atlantic area. The thin solid white line defines the plate boundaries and the thick solid white lines refine the Canadian and East European craton boundaries. The small orange circles represent the locations of known or proposed hotspots.

& Spakman (1999) use a large *P*-wave arrival time data set to derive a tomographic image beneath the North Atlantic, which shows a complex, low-velocity structure with numerous lateral branches extending from the upper mantle to the core–mantle boundary (CMB) beneath (CMB) most of the North Atlantic at the latitude of Iceland. Zhao (2001) invert *P*, *PP*, *pP* and *PcP* traveltimes and obtain a similar image. Shen *et al.* (1996, 1998) find the transition zone to be anomalously thin beneath Iceland and attribute this to hot material penetrating the transition zone from below. Helmberger *et al.* (1998) find evidence for an ultralow-velocity anomaly in the D″ layer beneath the North Atlantic and suggest that this may be associated with a CMB source of the Iceland plume.

Traveltime tomography studies using data collected on Iceland (e.g. Tryggvason *et al.* 1983; Wolfe *et al.* 1997; Foulger *et al.* 2001) are consistent with a strong, approximately 200-km-wide, low-velocity anomaly extending down to 400 km depth, the purported depth resolution limit of the seismic network, but there is no agreement on the shape of the low-velocity anomaly (Wolfe *et al.* 1997; Foulger *et al.* 2001). However, traveltime tomography studies using data collected on Iceland are hampered by the small aperture of the seismic network permitted by land-based seismographs and the poor distribution of regional earthquakes. For example, Keller *et al.* (2000) simulated a teleseismic body wave traveltime data set for Iceland based on the observations of Wolfe *et al.* (1997) and showed that, because of the relatively small aperture of the Icelandic seismic networks and the steeply arriving rays from the teleseismic sources, it is impossible to distinguish between a shallow, low-velocity anomaly in the upper 200 km and a cylindrical low-velocity anomaly extending to greater depth, suggesting that the actual depth resolution of the network is less than 400 km. Therefore, whether the source of the Icelandic plume is in the transition zone or deep mantle is still an open question.

In this paper, we present a high-resolution 3-D shear velocity and azimuthal anisotropy model for the upper mantle of the North Atlantic ocean and surrounding region from surface wave tomography. We used approximately 3000 multimode Rayleigh waveforms

recorded over relatively short paths compared with previous surface wave tomography models for the region. Employing short propagation paths in the analysis is advantageous because it minimizes artefacts in the tomographic model resulting from off-great-circle path propagation. The dense path coverage, wide azimuthal distribution, substantial higher mode content and short path-length of the data set have enabled us to build an upper-mantle model for the North Atlantic with a horizontal resolution of a few hundred kilometres extending to 400 km depth.

2 SURFACE WAVEFORM FITTING AND TOMOGRAPHY

We construct the 3-D upper-mantle Earth model following the two-step procedure used in a number of previous studies (e.g. Debayle & Kennett 2000; Priestley & Debayle 2003). Here, we discuss specific details of the method as applied to our study of the North Atlantic; a complete discussion of various aspects of the waveform inversion technique and the tomography can be found in Montagner (1986), Cara & Lévêque (1987), Lévêque *et al.* (1991), Lévêque *et al.* (1998), Debayle (1999), Debayle & Kennett (2000) and Pilidou (2004).

We first use the automated version (Debayle 1999) of the Cara & Lévêque (1987) waveform inversion technique to determine a 1-D path-average upper-mantle velocity model from each observed Rayleigh waveform. One important problem of waveform inversion is the highly non-linear relationship between a perturbation of the synthetic waveform and a perturbation of the elastic parameters describing the velocity model. To minimize this effect, Cara & Lévêque (1987) introduced the concept of secondary observables, which are built up from the seismograms using cross-correlation techniques. The secondary observables have only a weak non-linear dependence on the model parameters and therefore allow inversion with a standard non-linear scheme. For both the reference model used in determining the secondary observables and for the starting model in the inversion for the velocity structure, we use a smooth version of PREM (see Fig. 4)* (Dziewonski & Anderson 1981) for the mantle structure. For the crust we use a similar approach to that of Nolet (1990); we use a path-specific model determined by averaging the crustal part of 3SMAC (Nataf & Ricard 1996) along the path. We compute the source excitation for a point double-couple using source parameters taken from the Harvard CMT catalogue and the source region velocity structure of the 3-D 3SMAC model. The automated version of the Cara & Lévêque (1987) inversion code allows us to take advantage of the enormous volume of waveform data available to constrain the 3-D upper-mantle structure of the North Atlantic.

We then combine the 1-D velocity models in a tomographic inversion using a continuous formulation of the inverse problem (Montagner 1986; Debayle & Sambridge 2004) to obtain the local S_v-wave speed and azimuthal anisotropy at each depth. The formulation is based on the continuous form of the linear inversion scheme of Tarantola & Valette (1982). Lévêque *et al.* (1998) describe how the azimuthal anisotropy can be extracted in addition to the lateral variations in shear wave velocity from the 1-D path-average shear wave velocity model obtained from the Cara & Lévêque (1987) technique. They show that, in the long-period approximation and assuming a full but weakly anisotropic medium, the path-averaged shear velocity models depend on a combination of elastic parameters involving an isotropic term, which represents the lateral variation in shear wave velocity, and two anisotropic terms having an azimuthal variation in $\cos(2\theta)$ and $\sin(2\theta)$, where θ is the azimuth of the path. This azimuthal variation can be recovered by the Montagner (1986) approach provided a sufficient azimuthal distribution of paths is available.

The lateral smoothing in the tomographic inversion is controlled using a Gaussian *a priori* covariance function with a scale length L_{corr} and standard deviation σ. L_{corr} defines the distance to which adjacent points of the model are correlated and acts as a spatial filter; σ controls the amplitude of the perturbation in Earth structure allowed (velocity perturbation, azimuthal anisotropy, or both) in the inversion. The continuous regionalization approach used for the surface wave inversion provides an *a posteriori* error estimate for the extracted model, which is a useful guide to the resolution attainable from the data.

There are two underlying assumptions in the surface waveform tomography we employ: (i) the observed surface waves propagate between source and receiver along the great-circle path and (ii) they can be represented as multimode surface waves propagating independently. These assumptions are valid for a smoothly varying medium without strong lateral velocity gradients (Woodhouse 1974). Kennett (1995) examined the validity of the path-average approximation for surface wave propagation at a regional continental scale and concluded that this assumption is suitable for periods greater than 30 s and remains valid for periods longer than 50 s where surface waves cross major structural boundaries, such as continent–ocean transitions. Significant deviations from great-circle propagation have been observed for short-period (less than 40 s) surface waves (Alsina & Snieder 1996; Cotte *et al.* 2000), but surface wave ray tracing in Earth models (Yoshizawa & Kennett 2002) similar to ours confirms that off-great-circle propagation can be neglected for the fundamental and first few higher modes at periods greater than 40 s and for propagation paths less than 10 000 km without significantly affecting the resulting Earth model. Ritzwoller *et al.* (2002) examined the effects of off-great-circle propagation and found that for short path-lengths ($\sim$5000 km) the great-circle assumption was adequate but led to increasing bias in the inverted model as path-length increased. We therefore have attempted to restrict our analysis to relatively short paths while maintaining good azimuthal coverage.

Marquering *et al.* (1996) examined the effect of mode coupling. Body waves can be synthesized by summing large numbers of short-period higher mode surface waves, but the way in which body and surface waves sample the structure is different: surface waves are sensitive to the average structure along the propagation path, while body waves are most sensitive to the velocity structure near the geometrical ray turning point. In synthetic seismogram experiments, Marquering *et al.* (1996) found that when they used a large number (approximately 20) of modes including short periods (up to 10 s) and neglected mode coupling, the shallow parts of the inversion model that are sampled by the fundamental mode and the first few higher modes were reasonably accurate. However, they also observed that the deeper parts ($\sim$400 km) of the inversion model could differ significantly from the true model. To avoid artefacts in the model from neglecting mode coupling, we restrict our analysis to the fundamental and first four higher Rayleigh modes in the 50–160 s period band. Sensitivity kernels (e.g. see Debayle *et al.* 2001) show that using the fundamental and the first four higher modes in the 50–160 s period range achieves good sensitivity over the top 400 km of the upper mantle. Because the maximum sensitivity of the data for the fundamental mode and first few higher modes in this period

*In what follows, PREM refers to a smoothed version of the original PREM model: see Fig. 4, later.

range is sensitive to structure deeper than the Moho, we fix crustal structure to that of the 3SMAC model and invert only for the 1-D upper-mantle structure along the path.

3 DATA

The North Atlantic is well placed with respect to global seismicity for surface wave tomography studies. Large earthquakes occur over a wide range of azimuths at near-teleseismic distance and moderate earthquakes occur along the Mid-Atlantic ridge. We have assembled a data set of approximately 13 000 vertical-component Rayleigh wave seismograms with propagation paths crossing the North Atlantic from 622 events occurring in the period 1977–2002 recorded at 151 seismographs surrounding the North Atlantic (Fig. 2a). Approximately 75 per cent of these seismograms come from IRIS, GEOSCOPE and GEOFON stations; additional seismograms come from national seismic networks in Canada, the United Kingdom, Denmark (including stations in Greenland), Norway, Sweden and Iceland, temporary seismographs of the IRIS, PASSCAL, HOTSPOT and ICEMELT deployments in Iceland, and the Danish GLATIS deployments in Greenland (Fig. 2a).

To improve the path coverage, we installed additional stations in Iceland, along the east coast of Greenland, the Faeroe Islands, Ireland, Scotland and Norway (Fig. 2a) during 2000–2002 in places where there were gaps in the permanent station coverage. Most sites had a Guralp CMG3T sensor flat in velocity in the range 0.008–50 Hz, but a few had Streckeisen STS-2 sensors. The data were recorded on various data loggers. The stations in Norway were incorporated into the Norwegian national seismic network and stations in Iceland into the SIL network. Stations in the Faeroe Islands, Ireland, Scotland and Greenland were locally recorded on Reftek, Guralp SAM or Orion data loggers. All stations recorded data continuously and had GPS time.

Because the waveforms are automatically fit for each seismogram, the most important aspect of the analysis is the noise and error detection and data rejection procedures. For this we follow the automated procedure described in Debayle (1999). The first step of the process is to evaluate the bandwidth over which the seismogram can be analysed. Debayle (1999) initially proposed evaluating the signal-to-noise ratio at five different periods: 40, 60, 80, 120 and 160 s. The cross-correlograms used to calculate the secondary observables in the Cara & Lévêque (1987) approach are bandpass filtered around these different central frequencies before being inverted so the choice of the central frequencies defines the period bands in which each waveform is analysed. Debayle & Kennett (2003) compare tomographic results for Australia obtained by inverting the waveforms in the 40–160 and 50–160 s period bands and found little difference in the deeper part of the model (>130 km) for analyses from either band, but significant differences occuring at shallower depths. These differences are especially pronounced for the anisotropy pattern where shifts as large as 90° in azimuth occur in some parts of the model. Some of the discrepancy could be attributed to the increased resolution resulting from the inclusion of shorter wavelength 40-s waveforms, but part of the difference probably results from effects such as a departure from ray theory or an inaccurate crustal structure, both of which are more significant at the 40 s period. As the North Atlantic region encompasses large variations in crustal thickness, we choose more restrictive bandwidth criteria than Debayle (1999) and evaluate the signal in the 50, 70, 90, 120 and 160 s period bands. At each period, the signal-to-noise ratio is deemed adequate if the ratio between the maximum amplitude of the envelope of the signal and the maximum amplitude of the envelope of the noise is greater than 3.

From the signal-to-noise ratio evaluation, the automated waveform inversion chooses the bandwidth for the waveform analysis according to the following sequence of priority: (i) 50, 90 and 160 s; (ii) 50, 70 and 120 s; (iii) 50 and 90 s; (iv) 50 and 70 s. A

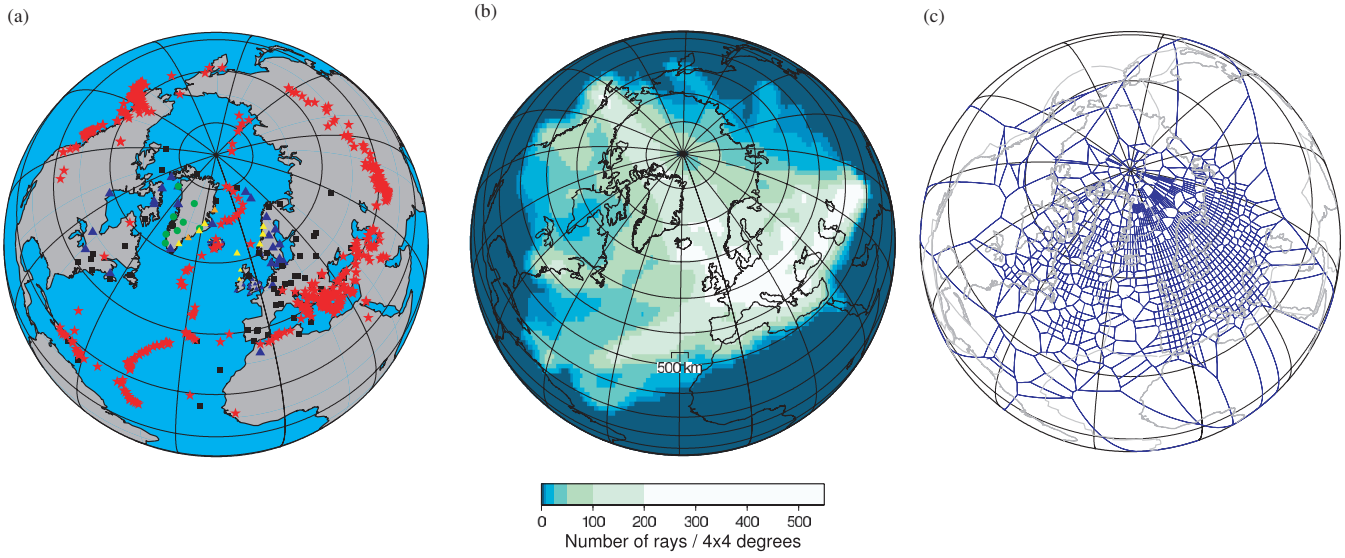

Figure 2. (a) Station and event locations. Red stars denote epicentres of events and all remaining symbols represent station locations: yellow triangles represent stations installed exclusively for this project, orange triangles represent the stations installed jointly with the Glatis project, solid green circles represent the Glatis project stations and black squares denote IRIS-IDA, IRIS-USGS, Gescope or Geofon permanent stations. Stations of the Canadian National Seismic Network, the Blacknest array in the UK, the Danish Seismological Network (in Denmark and Greenland), the Norwegian National Seismic Network, the University of Uppsala Network in Sweden, and the HOTSPOT, ICEMELT and SIL networks in Iceland are represented by the blue triangles. (b) Ray density (number of rays crossing 4° × 4° cells). (c) Voronoi cells (Debayle & Sambridge 2004): each cell represents the smallest area for which the $\cos(2\theta)$, $\sin(2\theta)$ azimuthal variation of S_v waves can be resolved.

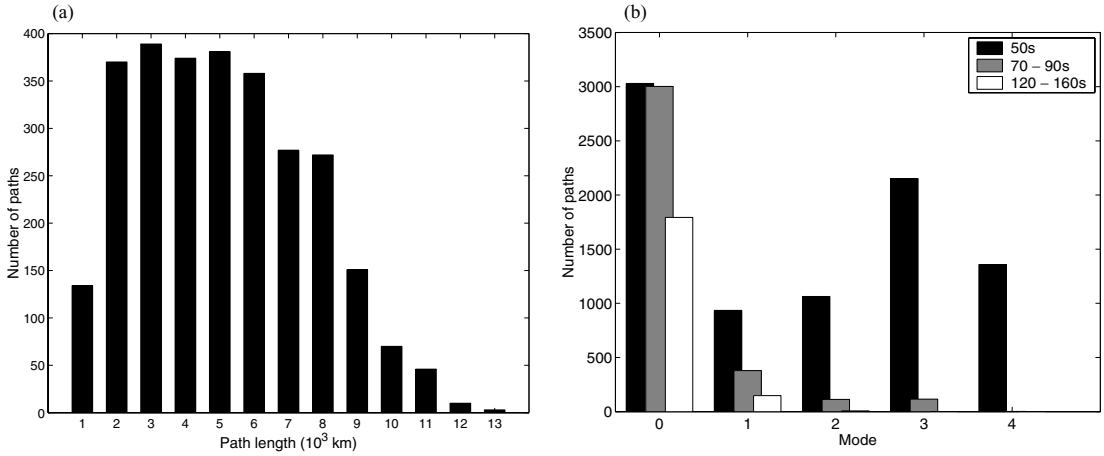

Figure 3. (a) Path length distribution and (b) number of seismograms analysed for the fundamental (0), first (1), second (2), third (3) and fourth (4) higher mode, in the frequency ranges of 50, 70–90 and 120–160 s.

minimum period range of 50–70 s is thus imposed for the waveform analysis. The use of a filtered cross-correlogram at the 60 s period is sufficient to constrain the S_v velocity at depths greater than 250 km, even when only the fundamental mode is used in the inversion (Lévêque *et al.* 1998). Once the bandwidth has been chosen, the automated waveform analysis is performed according to the procedure and criteria described in Debayle (1999). In particular, the inversion is considered successful if the final model provides a good fit to both the secondary observables and the observed seismogram and if the inversion has converged towards a stable velocity model.

This conservative procedure was used to build 3001 1-D path-average velocity models from which we construct the 3-D velocity and azimuthal anisotropy Earth model. The path density (Fig. 2b) is greater than 50 paths per $4^\circ \times 4^\circ$ square over a broad region around Iceland and Europe; the azimuthal distribution of paths is good, especially in the eastern North Atlantic and west central Europe (Fig. 2c). Fig. 3 shows the path-length distribution, and the frequency and modal composition of the data. The average propagation path-length in our study is 5141 km and very few of the path-lengths exceed 8000 km (Fig. 3a). While much of our data set consists of fundamental mode measurements, there is a significant higher mode content in the data set (Fig. 3b). However, the higher mode coverage is not uniform; for example, western Europe has denser higher mode coverage than the central North Atlantic ocean because of the numerous deep earthquakes in the Aegean and eastern Mediterranean.

Four examples of waveform fits before and after the 1-D waveform inversions and after the 3-D tomographic inversion are shown in Fig. 4 for a variety of epicentral distances and source depths. The 1-D waveform inversions achieve good waveform fits (Fig. 4 left) for both higher modes (clearly seen in Figs 4a and 4b), and the fundamental mode, despite the considerable misfit between the observed and initial synthetic seismograms. The waveforms calculated from the 3-D tomographic model (Fig. 4 right) are still in exceptionally good agreement with the observed waveforms.

4 TOMOGRAPHIC MAPS

The S_v-wave speed heterogeneity and azimuthal anisotropy maps for our North Atlantic model are shown in Figs 5 and 6. The background colour scale represents the variation in seismic wave speed and the bars represent the local direction of fast horizontal propagation of S_v waves. The length of the bars is proportional to the peak-to-peak azimuthal anisotropy. If the upper-mantle anisotropy primarily results from the preferred alignment of olivine crystals, the direction of fast S_v-wave propagation is expected to be along the projection in the horizontal plane of the fast α-axis of olivine (Lévêque *et al.* 1998).

The model shown in Fig. 5 was obtained using $L_{\rm corr} = 400$ km for both velocity heterogeneity and azimuthal anisotropy, $\sigma = 0.05$ km s^{-1} for the velocity perturbation and $\sigma = 0.003$ km s^{-1} for the azimuthal anisotropy variation. This choice favours a smooth model considering our shortest wavelengths (approximately 200 km at a 50 s period) and dense path coverage. We tried various values of $L_{\rm corr}$ but even with $L_{\rm corr} = 1000$ km, we found the inversion model was smoother than the model shown in Fig. 5 but that the main features of the model were essentially the same. The synthetic tests discussed below show that the path density (Fig. 2b) and *a priori* information allow us to resolve structures with horizontal wavelengths of a few hundred kilometres for the uppermost 400 km of the model. This agrees with the lateral resolution that can be expected when considering the influence zone over which surface waves are coherent in phase and that is identified as approximately one-third of the first Fresnel zone (Yoshizawa & Kennett 2002). In the region lying outside the influence zone, scattering effects, such as multipathing, can become important (Spetzler *et al.* 2002), but in general we did not observe evidence of multipathing in the part of the waveforms we analysed. This suggests that ray theory applies in our period range of analysis.

The *a posteriori* error maps (Fig. 7) display a pattern very similar to that of the path distribution (Fig. 2b) and optimum Voronoi (Fig. 2c) diagrams. The grey areas in Fig. 5 denote regions with an *a posteriori* error greater than 0.04 km s^{-1} and correspond to regions of poor resolution, i.e. regions where the *a posteriori* error is close to the *a priori* error (0.05 km s^{-1}). The resolution is best where the *a posteriori* error is small. The *a posteriori* error maps and profiles (Figs 7 and 8) show that the resolution is significantly better in central Europe, especially at depth, than in the central Atlantic ocean. The good depth resolution in central Europe is clear from profile EE′ (Fig. 8).

The model maps (Fig. 5) show a high degree of S_v-wave speed heterogeneity (± 8 per cent) and large amplitude (up to 3 per cent) and complex pattern of azimuthal anisotropy in the shallow (75–150 km depth) layers. Both the amplitude of the S_v-wave speed

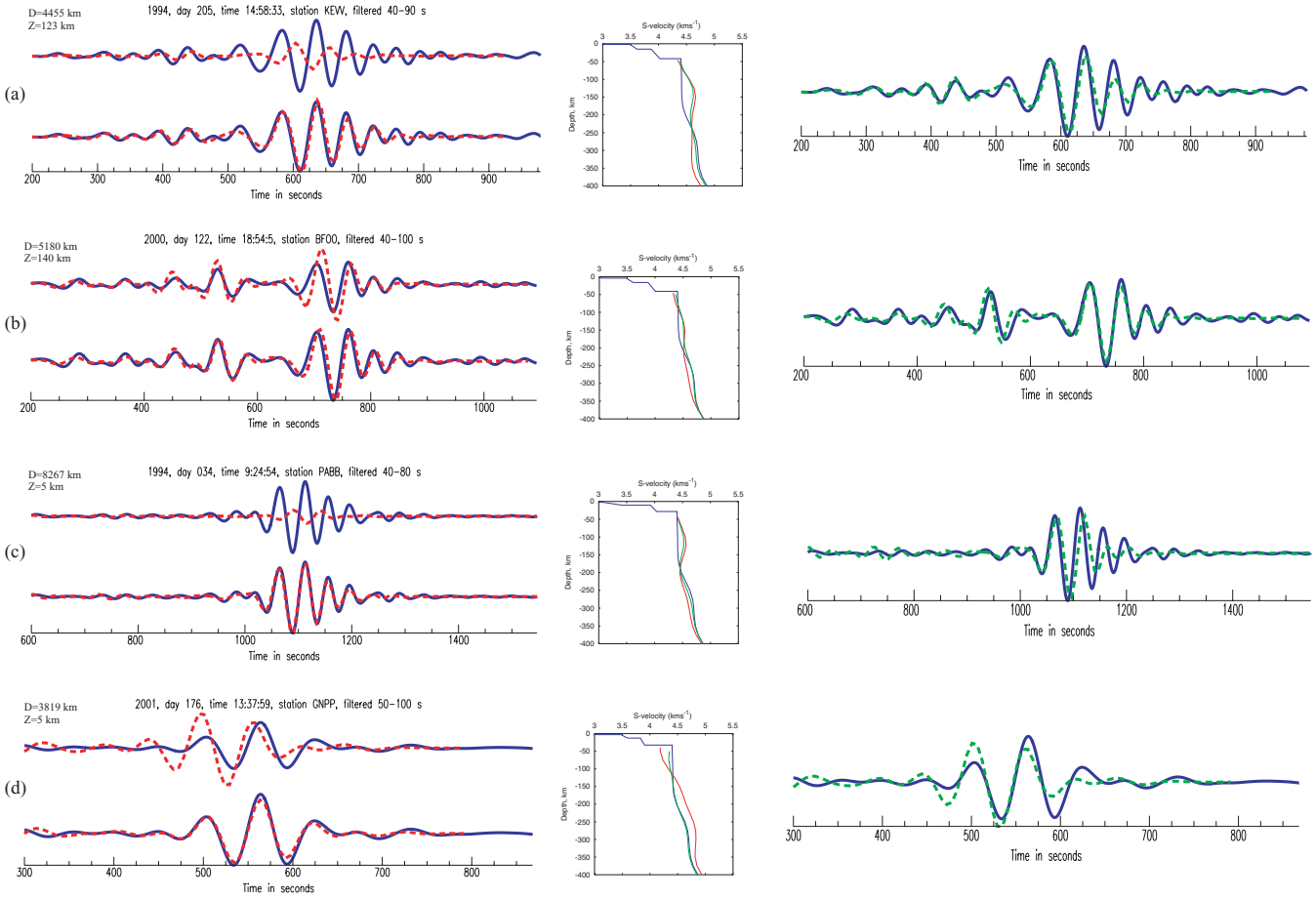

Figure 4. Waveform fits and the resulting 1-D path-averaged S_v models after the 1-D-inversions (left) and fits for the same paths after the 3-D tomographic inversion (right). The observed seismograms are denoted by the blue solid lines in both cases. Left: the top and bottom traces are the fits before and after the 1-D waveform inversions, respectively. The epicentral distance, D, and focal depth, Z, are shown at the top left corner of each plot. Waveforms (a), (b), (c) were recorded by permanent Global Digital Network stations, whereas waveform (d) was recorded by the station GNP, which we deployed in Ireland. Dashed red lines denote the synthetic seismograms. Right: dashed green lines denote the synthetic seismograms calculated from the 3-D model shown in Fig. 5. Middle: S_v models; the initial model (3SMAC crust and smoothed PREM mantle) is denoted by the solid blue line, the final 1-D waveform inversion model is denoted by the red line and the 1-D path-averaged model calculated from the 3-D model shown in Fig. 5 is denoted by the green line.

heterogeneity and the complexity and amplitude of the azimuthal anisotropy decrease with depth. In the deeper parts of the model (>200 km depth) the S_v-wave speed heterogeneity is reduced to ±2.5 per cent and the amplitude of the azimuthal anisotropy to 1 per cent.

As discussed in Section 6, there are a number of well-known features in our mantle model, such as the high-velocity roots beneath the Canadian and Greenland shields in North America and beneath the Baltic shield and the East European platform in Europe (Fig. 1). Three major hotspots occur in the region covered by our model: Iceland, the Azores and Eifel. Low-velocity anomalies occur in the upper mantle beneath each of these hotspots. Iceland is located on the Mid-Atlantic ridge and the Azores are located near the ridge. The upper-mantle low-velocity anomalies beneath both these hotspots are elongated along the direction of the ridge and extend to approximately 200 km depth. There is no evidence of a slow anomaly extending deeper than 200 km. The Eifel hotspot is located in NW Europe, a slow moving plate. In this area of the model, we have the best depth resolution (Figs 7 and 8). The low-velocity anomaly beneath the Eifel hotspot is roughly circular and extends to the bottom of the model at 400 km depth.

We discuss in more detail the low-velocity structures associated with these three hotspots in Section 6. In the following section we discuss the reliability and resolution of our model based on several synthetic seismogram experiments.

5 RELIABILITY AND RESOLUTION OF THE 3-D MODEL

There are a number of factors that could introduce artefacts and bias into the tomography model. These include errors in the theory and approximations such as assuming great-circle propagation, neglecting mode coupling and using an inappropriate starting model for the inversion, poor knowledge of the non-inverted parameters such as the earthquake hypocentral coordinates and focal mechanism, the fixed crustal model and poor path coverage. As discussed above, errors in the tomographic model resulting from the great-circle approximation are minimized by choosing relatively short propagation paths. Artefacts in the tomographic model resulting from ignoring mode coupling are minimized by considering only the fundamental and first four higher modes for periods greater than 50 s.

Cara & Lévêque (1987) show that for their waveform inversion technique, the final velocity structure is weakly dependent on the

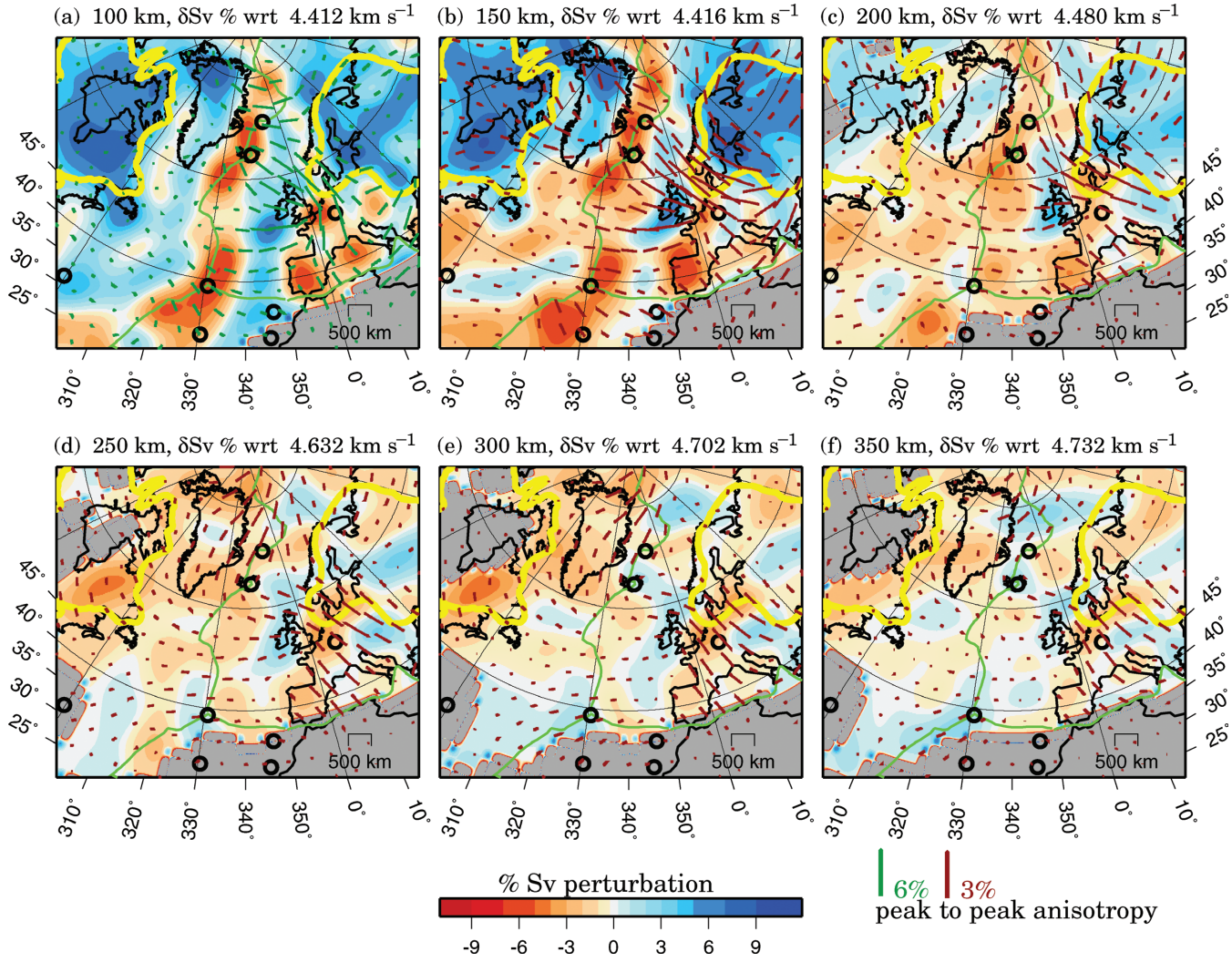

Figure 5. S_v-wave heterogeneity and azimuthal anisotropy distribution at depths of (a) 100, (b) 150, (c) 200 (d) 250 (e) 300 and (f) 350 km. The heterogeneity is shown as the departure from a smooth PREM mantle model. Red and blue colours represent areas of slower and faster velocities, respectively with respect to the reference model. The fast directions of horizontally propagating S_v waves are shown by the light green (a), or red (b–f) bars, the length of which is proportional to the peak-to-peak azimuthal anisotropy. The solid green line defines the plate boundaries and the solid yellow lines refine the Canadian and East European craton boundaries. Areas shaded in grey correspond to regions of *a posteriori* error greater than 0.040 km s^{-1}. The error distribution is shown in Fig. 7. The depths and reference velocities are indicated at the top of the plots. The vertical cross-sections along the profiles marked on map (a) are shown in Fig. 6. See also Fig. 9 for the results at the depths of 75 and 125 km.

reference and inversion starting model. Errors in source parameters will cause errors in the 1-D path-average velocity models (Ritzwoller & Levshin 1998; Maggi & Priestley 2003). Ritzwoller & Levshin (1998) examined the effect of a systematic shift in event locations on regional scale tomography and found that if the path density and azimuthal coverage is good, the effects of the mislocation were restricted to the source region and were of small magnitude. In the present study, we believe that there is no reason for these effects to be coherent because they relate to earthquakes with different source mechanisms covering a wide area; the errors are expected to average out in the tomographic inversion if, as in this study, a large number of paths with different azimuths are used to constrain structure. In the following sections, we evaluate other possible factors affecting the reliability and resolution of our tomographic model for the upper mantle beneath the North Atlantic.

5.1 Influence of the fixed crustal structure

The long-period surface waveforms we invert are sensitive to the structure of the crust, but are of too long a wavelength to constrain the crustal structure. Therefore, in the 1-D waveform inversion we assume a crustal model by averaging the crustal part of the 3SMAC model (Nataf & Ricard 1996) along the propagation path, then keep the crustal structure fixed while inverting for the mantle structure. Poor constraints on the fixed crustal structure can bias the mantle structure. To assess the validity of our choice of the 3SMAC model, we reinverted the complete waveform data set using an updated version of CRUST2.0 (Bassin *et al.* 2000) as a starting model for the average crustal structure beneath each point. We updated the CRUST2.0 for the North Atlantic region using the results of Dahl-Jensen *et al.* (2003) for Greenland; the results of Darbyshire

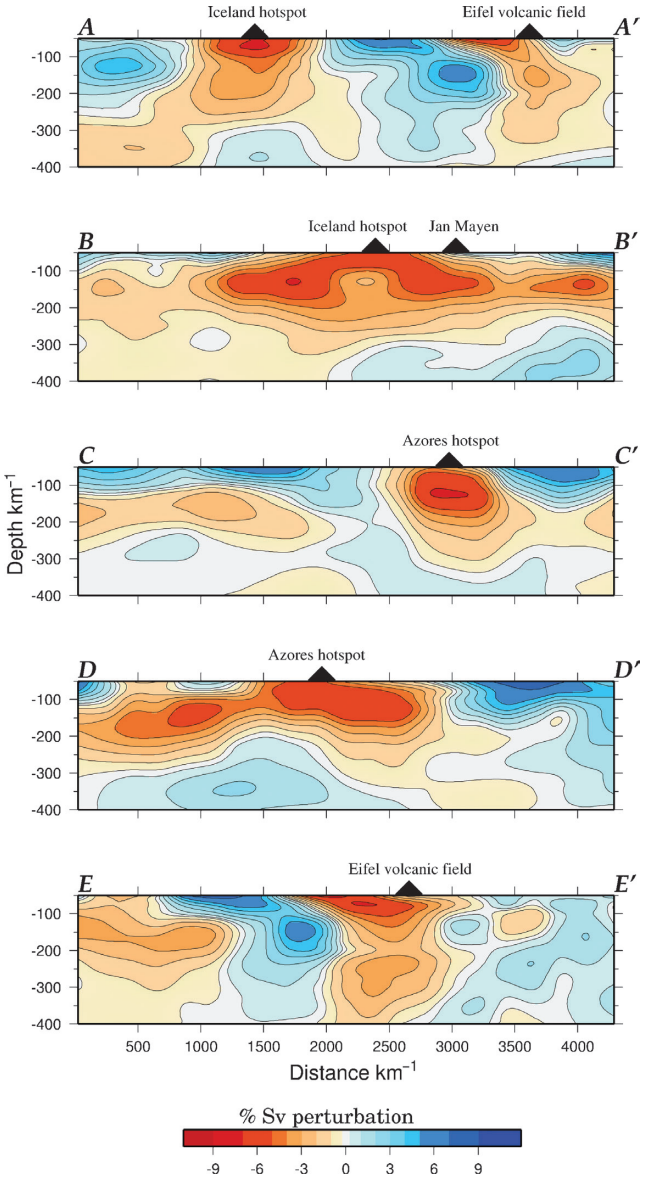

Figure 6. Vertical cross-sections along the 4300-km-long profiles AA′–EE′, marked on Fig. 5(a).

et al. (2000b), Kaban *et al.* (2002) and Gudmundsson (2003) for Iceland and the surrounding plateau and the results of White *et al.* (1992) for the thickness and internal layering of oceanic crust around Iceland. We moved the CRUST2.0 location of the Rockall plateau and the Norwegian basin to more accurate locations. Crustal velocities and densities were not modified except at continental/oceanic boundaries and in the area of Iceland where evidence suggests that the thick crustal root is unusually dense and fast (Darbyshire *et al.* 2000b; Gudmundsson 2003).

Fig. 9 compares the mantle structures obtained at 75 and 125 km depth when the 3SMAC and updated CRUST2.0 models are used for the crustal structure. Both the positive and negative anomalies in the inversion using CRUST2.0 are somewhat stronger in amplitude but smoother than the anomalies in the tomographic model derived assuming the 3SMAC crust. The anisotropic pattern remains essentially the same, especially in the better resolved parts of the model (Fig. 2c). However, we observe locally some differences in the amplitude of anisotropy, especially in the shallow part of the model (<100 km depth). In general, most differences between the two inversions occur at shallow depths (<100 km) where the images obtained assuming CRUST2.0 are less complex and have a stronger resemblance to the surface tectonics than the image obtained using 3SMAC. The choice of crustal model has little effect on the upper-mantle model at depths greater than 100-km mantle.

5.2 Resolution tests

We performed a number of synthetic seismogram experiments to test the resolution of the S_v wave speed heterogeneity attained in the model. The resolution is controlled by the density and azimuthal distribution of the paths and the frequency content and modal composition of the surface waves. In each test, we calculate multimode synthetic seismograms for propagation paths through a simple 3-D input model for the same source parameters and event–receiver combinations as in the actual data. The synthetic surface waveforms are analysed in exactly the same way as the actual data using the automated analysis procedure outlined in Section 2. Because we invert the synthetic seismograms for the same frequency content and mode combinations as in the real data (Fig. 3), our tests not only provide information on the spatial resolution of the model from the path coverage, but because we repeat the 1-D inversion step the tests also provide information on the depth resolution.

We use a traditional checkerboard test to evaluate how well the 3-D tomographic images reflect the shapes and amplitudes of a given distribution of shear velocity heterogeneity. For this test, we use an input model consisting of a regular pattern of alternating velocity perturbations to generate a synthetic data vector with the same path distribution as the real data; then the synthetic data vector is inverted in the same way as real data. It is commonly assumed that regions of the model where the synthetic pattern is faithfully recovered by the inversion correspond to regions where the Earth structure is well recovered in the inversion of the actual data, at least for perturbations of similar or greater size. Lévêque *et al.* (1993) show that this intuitive interpretation of checkerboard tests is dangerous and the resolution of fine features of the synthetic model does not necessarily imply equally good resolution of coarser features: each test reveals only the resolution of perturbations with that particular input scale. The results of checkerboard tests primarily reflect the path coverage and do not account for true data noise, errors in earthquake source parameters or deviation from underlying assumptions of great-circle propagation and the lack of mode coupling. However, the checkerboard tests shown in Figs 10 and 11 give an impression of the resolution achieved by the path geometry in conjunction with the final model smoothing.

In the first test, we use an input checkerboard model consisting of blocks $10^\circ \times 10^\circ$ in horizontal and 100 km in vertical dimensions, with a ± 6 per cent velocity perturbation with respect to PREM. Horizontal slices and vertical cross-sections of the recovered checkerboard models are shown in Figs 10(a), (b), (c) and 11(a). In the area of good path coverage (Fig. 2b and c), the input model geometry is well recovered at all depths. The amplitude reconstruction is very good at depths shallower than 150 km in the model, while at larger depths the anomalies decay in magnitude. Fig. 11(a) shows cross-sections through the recovered checkerboard models corresponding to profiles similar to the ones through the model shown in Fig. 5(a). These more clearly demonstrate that the depth geometry of the input model is generally well recovered and also that the amplitude recovery decreases with depth. The deep structure is most faithfully recovered along profile EE′ (Fig. 11a) because of the dense higher mode coverage in western Europe.

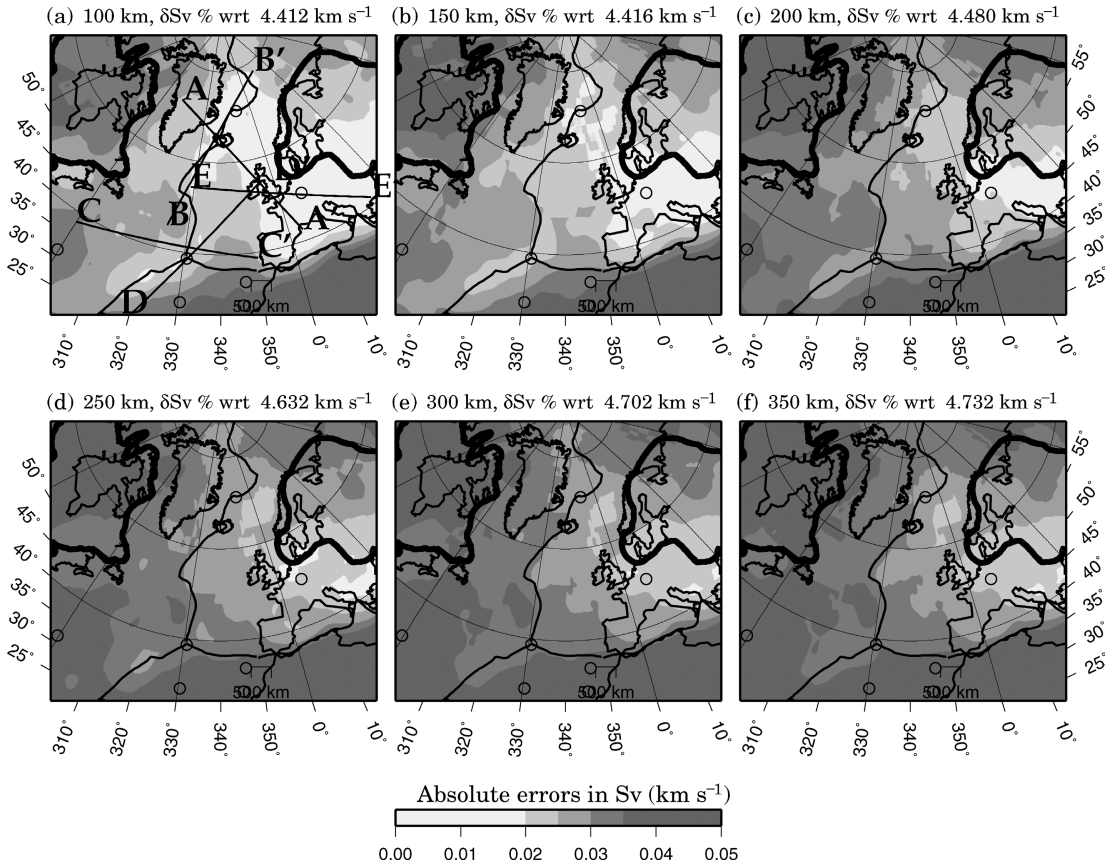

Figure 7. *A posteriori* absolute error distribution of S_v for the sections shown in Fig. 5. The *a priori* error was set to 0.05 km s^{-1}. The darker areas (error greater than 0.04 km s^{-1}) correspond to areas of lacking resolution and correlate with the ray density distribution shown in Fig. 2. The depth is indicated above each plot.

Figs 10(d), (e), (f) and 11(b) show the recovery of a 7° × 7° checkerboard for the same depth slices and vertical cross-sections. Where the path density and azimuthal coverage are high, the geometry of the structure is well recovered in the shallow (<150 km) part of the model, but the recovery is noticeably worse in the deeper part of the model. However, even with the 7° × 7° checkerboard, the resolution beneath central Europe is good as a result of the higher density of higher mode paths across this region from the subcrustal events in the eastern Mediterranean.

We perform a second synthetic seismogram experiment to determine whether the amplitude decay with depth of the low-velocity anomaly associated with the Iceland plume (sections AA′ and BB′ of Fig. 6) is real or an artefact resulting from the specific frequency and higher mode content of our data set. The input model consists of a low-velocity (−5 per cent perturbation with respect to PREM) cylinder, 1000 km in diameter, extending from 50 to 600 km depth, centered on Iceland and embedded in a smoothed PREM mantle structure (Fig. 12). There is significant decay in amplitude of the cylinder with depth in the recovered model, but the decay is much more gradual than that of the low-velocity feature beneath Iceland seen in our model (Fig. 6), suggesting that this broad low-velocity anomaly does not extend to a depth greater than 200 km, because such a broad structure would have been resolved by our long-period and higher mode data set.

In a third synthetic experiment, we try to determine whether a narrow, plume-tail structure, 200 km wide, beneath Iceland could be resolved with our data set. The synthetic experiment is conducted in the same way as the two previous experiments but using a plume-like (e.g. Watson & McKenzie 1991) structure as a starting model, consisting of a 1200-km-diameter cylinder extending from 50 to 200 km depth (the plume head) above a 200-km-diameter cylinder extending to 600 km depth (the plume stem; Fig. 13a). This structure is centered on Iceland (65°N, 20°W) and has a velocity perturbation of −5 per cent with respect to PREM. The recovered model (Fig. 13b) is a smoothed and symmetrically smeared version of the input structure. We recover a smooth version of the plume head structure with a central amplitude anomaly of approximately −5 per cent. The presence of the plume stem is detected, but its exact shape and amplitude are not properly resolved, as might be expected because the horizontal smoothing ($L_{\rm corr}$ = 400 km) introduced in the inversion is twice the width of the stem. In the region of the plume tail we recover an amplitude of 1 per cent. This corresponds to a velocity perturbation of 0.045 km s^{-1} which is at the limit of the resolution in this part of the model as shown by the *a posteriori* error on profiles AA′ and BB′ in Fig. 7. Therefore, the fact that we do not observe a narrow, low-velocity feature below 200 km in the upper mantle does not rule out the existence of a plume tail at depths deeper than 200 to 250 km beneath Iceland. Fig. 13(c) shows the results of the same tomographic inversion but with $L_{\rm corr}$ = 100 km. The plume stem in this test is more localized but the amplitude is weak (<1 per cent) suggesting that the limiting factor is the lower density of higher mode paths for this part of the structure.

5.3 Azimuthal anisotropy test

The last series of synthetic seismogram experiments is designed to test both the resolution of azimuthal anisotropy and the

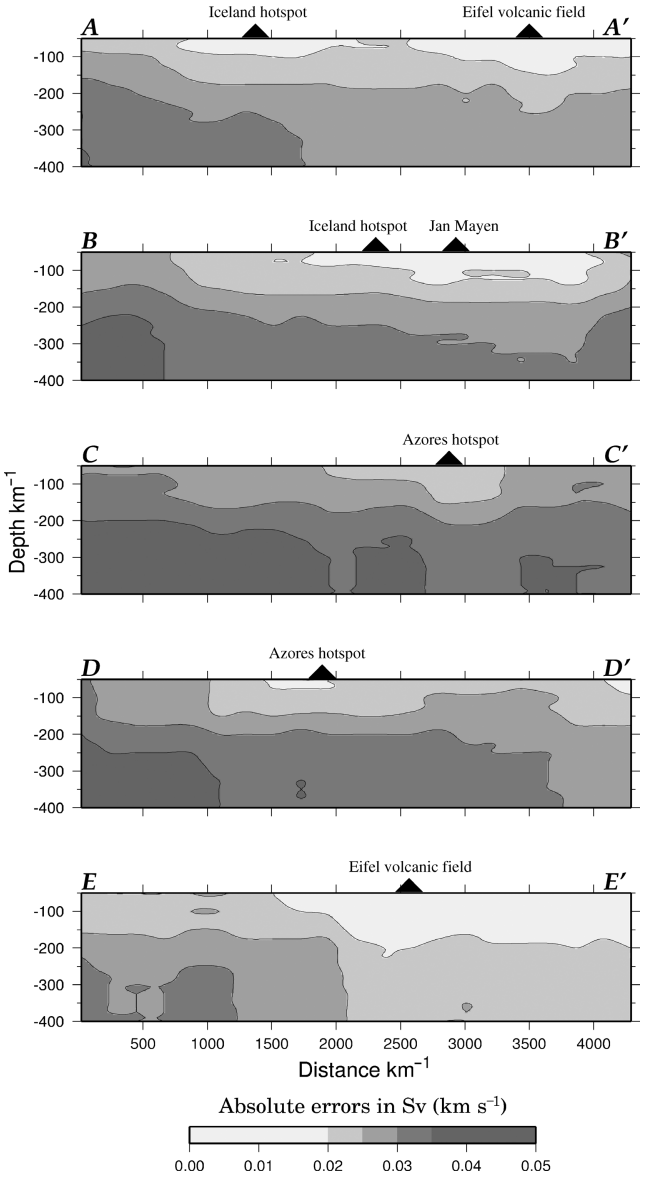

Figure 8. Posterior S_v error distribution for the profiles shown in Fig. 6.

magnitude of trade-off between heterogeneity and azimuthal anisotropy. In the first experiment, we construct a homogeneous input model (smoothed PREM) in which we add a pattern of azimuthal anisotropy with a peak-to-peak amplitude of 5 per cent with a pattern for the fast anisotropy that displays an abrupt change in direction. The input model and inversion results are compared in Fig. 14. The magnitude and direction of the anisotropy pattern is in general well reconstructed in areas of good azimuthal coverage (Fig. 2). In the region of abrupt change in anisotropic direction, the horizontal smoothing introduced by the long-period surface waves can, however, produce locally an anisotropic pattern that is wrong in both amplitude and direction. This is particularly clear in Fig. 14(d) in the region located near the Mid-Atlantic ridge to the west of Europe and in Fig. 14(f) in the region around 50°N. This suggests that the anisotropic pattern obtained with surface waves can be locally wrong in regions where changes in anisotropic direction would occur over distances much smaller than a wavelength. For this reason, we will discuss only the general trend of the anisotropy and not the fine details of the anisotropic direction in the next section. Fig. 14 also indicates that there is a coupling between azimuthal anisotropy and lateral heterogeneity with as much as ±2 per cent lateral heterogeneity arising from the azimuthal anisotropy.

In the second experiment, we use the 3-D heterogeneous isotropic 3SMAC mantle model for the input model (Figs 15a and b) and allow for both heterogeneity and azimuthal anisotropy in the tomographic inversion. The heterogeneity is well reconstructed (Figs 15c and d) and the magnitude of the anisotropy is everywhere smaller than approximately 0.7 per cent at 100 km depth and decreases deeper in the model. However, the anisotropy pattern appears to be region-dependent. In the ocean, the fast propagation direction changes from E–W north of approximately 70° to NW–SE south of this. It strikes E–W in the Greenland and the East European platforms and changes to roughly N–S in west Europe in the areas of the Eifel hotspot and the Iberian peninsula. The fast polarization direction in west Europe is similar to the fast polarization direction we observe in our model (Fig. 5a), but is of much smaller magnitude.

From these anisotropy experiments, we conclude that 5 per cent peak-to-peak anisotropy can result in 2 per cent heterogeneity, whereas 6 per cent heterogeneity can result in 0.7 per cent peak-to-peak anisotropy. This places bounds on the magnitude of the azimuthal anisotropy we can interpret in our model.

6 DISCUSSION

6.1 Shear velocity heterogeneity

The tests we performed show that our tomographic model for the North Atlantic and surrounding region is reliable and robust. The upper-mantle structure at depths greater than 100 km is not likely to contain significant artefacts resulting from our choice of a fixed crustal model. The synthetic tests suggest that input heterogeneities with wavelength of 700–1000 km should be well recovered both laterally and vertically throughout the model down to 400 km depth. The amplitude of the anomalies is well recovered in the upper 200 km of the model, but the amplitude of features is increasingly underestimated with increasing depth. Azimuthal anisotropy is well resolved in the areas of good azimuthal path coverage, including the area around Iceland. From our synthetic tests, we do not expect a trade-off between heterogeneity and anisotropy higher than 2 per cent.

The high-velocity lids associated with continental cratons are clearly visible in our model. There is not sufficient resolution at depth beneath the western edge of our model to image the bottom of the Canadian Shield, but high velocities extend to approximately 200 km depth beneath most of Greenland. The high-velocity root beneath the Baltic shield and the East European platform persists to approximately 250 km depth. At 150 km depth there is a well-defined boundary between the high velocities observed beneath the East European platform and low velocities observed beneath the tectonically younger parts of central Europe, coinciding with the Tornquist–Teisseyre zone as previously noted in the studies of Zielhuis & Nolet (1994), Marquering & Snieder (1996) and Marquering *et al.* (1996). There is a clear thickening of the oceanic lithosphere with increasing distance from the mid-ocean (Zhang & Lay 1999). Low upper-mantle velocities exist beneath the Iberian peninsula, as also previously noted by (Marquering & Snieder 1996), and beneath the Tyrrhenian basin, as also seen in the models of Silveira & Stutzmann (2002) and Faccenna *et al.* (2003). The low-velocity anomaly beneath the Iberian peninsula could be related to a convective upwelling in the mantle and the cause of the high elevation of the Iberian Peninsula (Dan McKenzie, private communications, 2003)

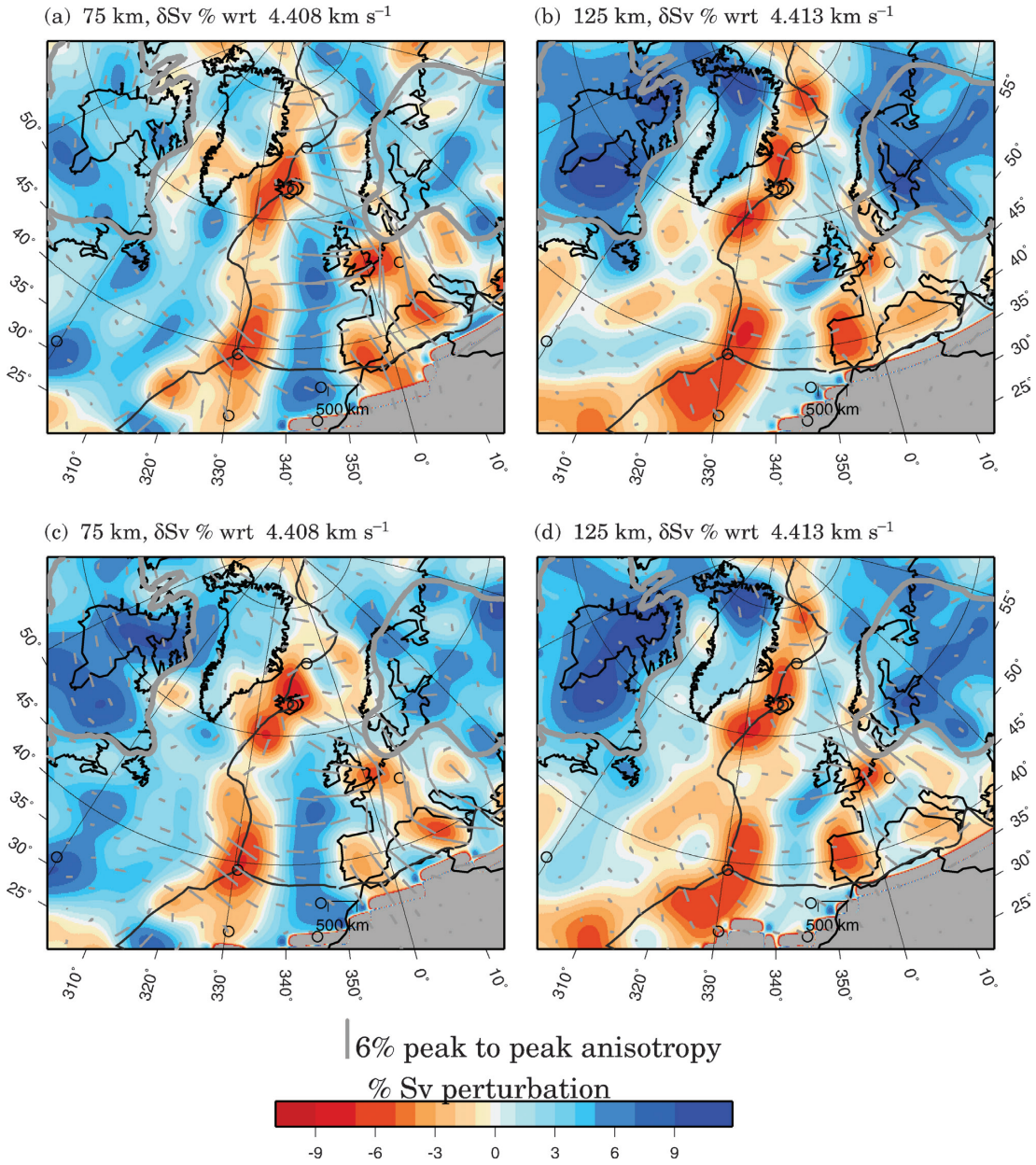

Figure 9. S_v wave heterogeneity and azimuthal anisotropy distribution at depths of (a) 75 and (b) 125 km. The results at the same depths, but using an updated model for the crust based on the CRUST2.0 model (see Section 5.1 for details) are shown in (c) and (d). The figure convention is the same as that of Fig. 5.

6.1.1 The Iceland plume

The Iceland plume has a high buoyancy flux (Sleep 1990) and is centred beneath the Mid-Atlantic ridge, which is slowly spreading at a rate of 1.9 cm yr^{-1} (full-spreading rate). The upper-mantle low-velocity anomaly associated with Iceland has a plume-head-like structure (Watson & McKenzie 1991) of varying diameter and extends to a depth of approximately 200 km (Fig. 6, profiles AA′ and BB′). At 75 km depth (Fig. 9), the shape of the low-velocity anomaly is roughly circular with a diameter of approximately 1000 km, the S_v velocity is 5–7 per cent slower than PREM and the anomaly is approximately centered on Iceland. By 100 km depth, the low-velocity anomaly is elongated along the direction of the Mid-Atlantic ridge with dimensions of approximately 2000 km along the ridge and 600 km perpendicular to the ridge. The low-velocity anomaly both thickens and deepens north and south of Iceland (Fig. 6, BB′). Below 175 km depth the low-velocity anomaly decays to the PREM background level at 200–225 km depth.

Between approximately 75 and 175 km depth the wave speed in the low-velocity anomaly has an almost constant S_v velocity of 4.10 ± 0.05 km s^{-1}. Priestley & Tilmann (1999) found the same velocity in this depth range beneath Hawaii, another large plume with a heat flux similar to that of Iceland (Sleep 1990). The observed velocities at these depths beneath Hawaii are slightly lower than the shear wave velocity thought to occur in the asthenosphere beneath 0–20 Myr oceanic lithosphere (Nishimura & Forsyth 1989) of the fast-spreading Pacific ridge. Priestley & Tilmann (1999) attributed these low velocities to plume material ponding beneath the plate. The low velocity observed beneath Iceland is averaged over a distance of 400 km centered on Iceland (Fig. 6, profile AA′). Because the

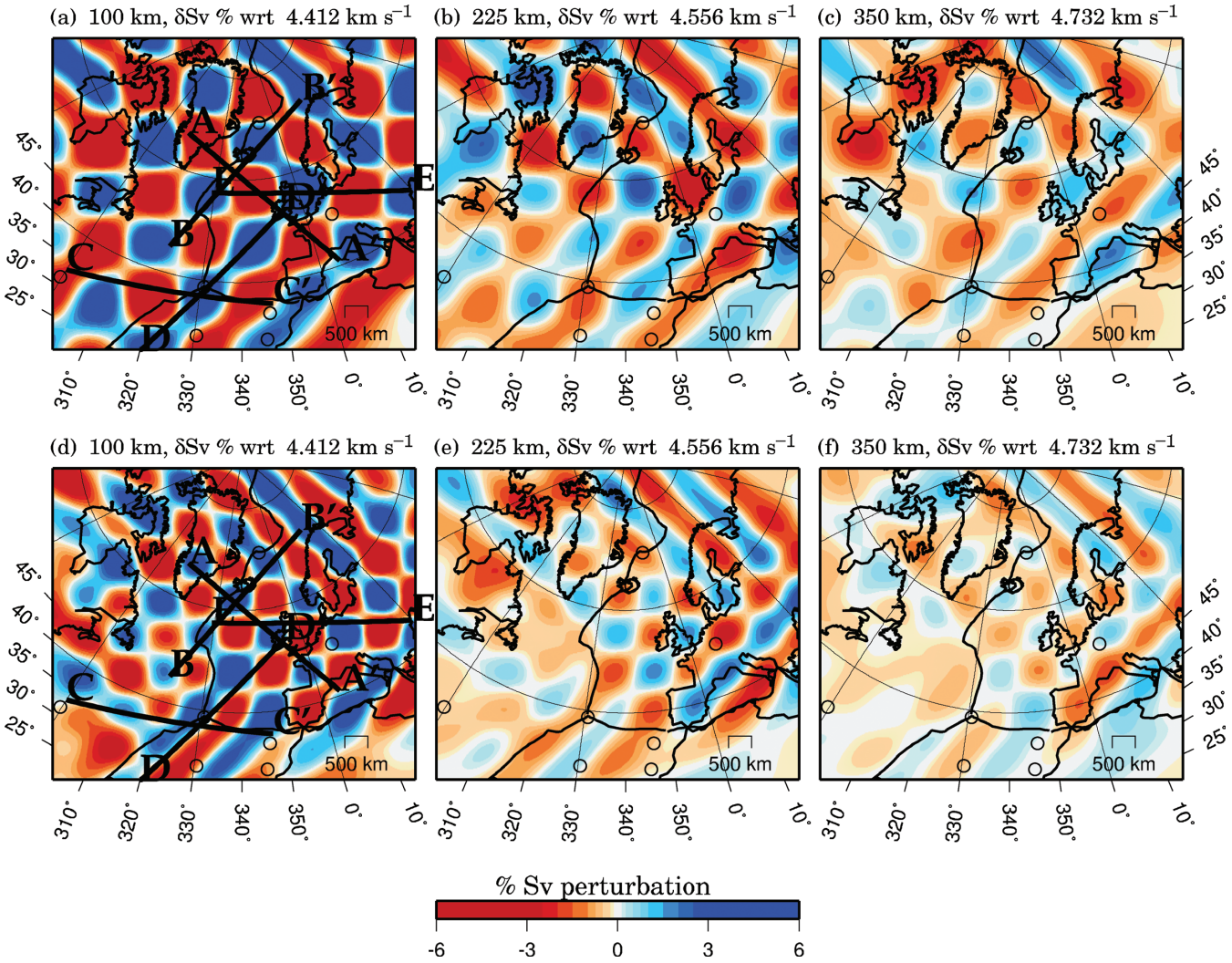

Figure 10. Recovered models from two synthetic seismogram experiments. The input model is a 3-D checkerboard structure, with 3-D blocks of alternating magnitudes ±6 per cent, vertical extents of 100 km and horizontal extents of 10° × 10° (a–c) and 7° × 7° (d–f). The vertical sections through the models along the profiles marked on maps (a, d) are shown in Fig. 11.

Mid-Atlantic ridge is spreading at a slower rate than the Pacific, the velocity beneath Iceland is averaged over a broader age range and is therefore expected to be higher than that observed beneath Hawaii, given that the two plumes have similar strengths. The mantle velocity beneath Iceland is therefore clearly anomalously low for the slow-spreading Atlantic ridge. Similar low shear wave velocities were found by Allen *et al.* (2002b) between the Moho and 200 km depth in a more restricted region beneath Iceland.

The observed low-velocity anomaly we observe in the North Atlantic beneath Iceland has a significantly larger NS dimension along the ridge axis than the EW dimension perpendicular to the ridge axis. Numerous observations indicate that the Reykjanes ridge segment of the Mid-Atlantic ridge south of Iceland is modified by the plume. For more than 1000 km to the south of Iceland the seafloor is anomalously shallow (Vogt 1971), the topography is much smoother and lacks segmentation and an axial valley typical of slow-spreading ridges (Searle *et al.* 1998), and the crust is anomalously thick (Smallwood & White 1998). Gravity and bathymetry data show prominent *V*-shaped anomalies (Vogt 1971) along the ridge, which correlate with local variations in crustal thickness. Isotope and trace element ratios measured along the Reykjanes ridge are different from those measured along ridge segments located away from active plumes and indicate a mixing of an enriched plume source and Mid-ocean ridge basalt (MORB) source (Schilling 1973; Fitton *et al.* 1997). All these observations are indicative of plume material flowing laterally along the ridge, from the plume centered beneath Iceland. Gaherty (2001) found that Rayleigh waves propagating south of Iceland along paths parallel to the Reykjanes ridge arrived at the predicted time but Love waves arrived late, indicating anisotropy but of the opposite sign to that normally observed for Rayleigh and Love waves. He attributed this unusual form of anisotropy to the supply of heat beneath the ridge, producing excess buoyancy driving a sheet-like mantle upflow beneath the ridge to a depth of approximately 100 km. The *V*-shaped gravity, bathymetry and crustal thickness variations along the ridge are thought to reflect a time variation of the Iceland plume (Vogt 1971).

Alber & Christensen (2001) investigate the interaction of a mantle plume with a mid-ocean ridge in a 3-D numerical modelling experiment, using a strongly temperature-dependent viscosity model. They investigate how the shape and dimensions of a plume head depends on the various model parameters and find that, for a strong, plume-like structure beneath a slow-spreading ridge, the plume

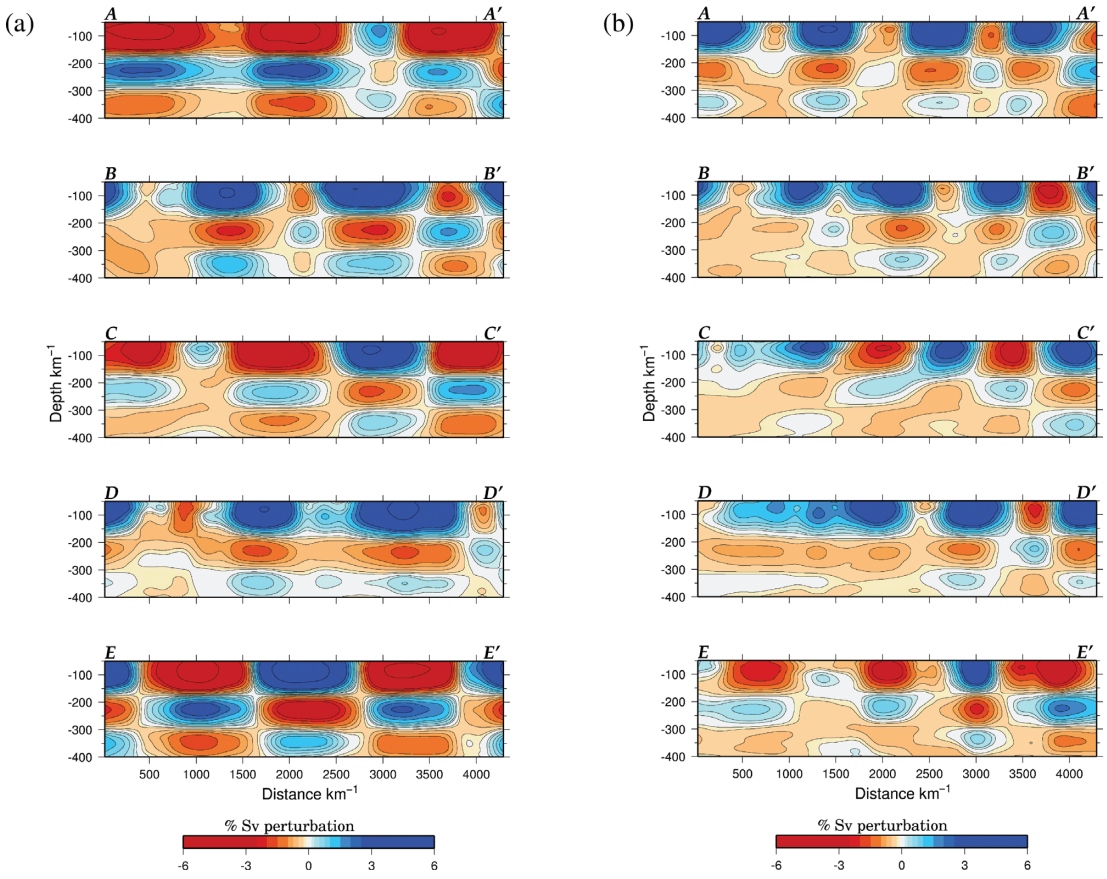

Figure 11. (a, b) vertical cross-sections along the 4300-km-long profiles AA' to EE', marked on Figs 5(a) and (d), respectively.

material rises to the base of the plate and spreads laterally but preferentially along the ridge axis. The thickening lithospheric plate perpendicular to the ridge forms an upper boundary of an elongated wedge-shaped region, which confines the material in the plume head, causing most of the plume material to flow along the ridge until it cools and becomes part of the newly generated lithosphere. Sleep (1996) compares the flow pattern of plume material beneath ridges with the analogy of an upside-down drainage pattern. Using a model plume with the parameters appropriate for the Iceland plume, Alber & Christensen (2001) find the along-axis plume dimension to be 1800 km and the aspect ratio (ratio of along-ridge to across-ridge length) to be 3.16. At 100 km depth the low-velocity feature centered beneath Iceland extends from approximately 54°N to 70°N, with a total length of approximately 2000 km and width of approximately 600 km, corresponding to an aspect ratio of 3.3.

The low-velocity anomaly in the north of Iceland, along the Kolbeinsey ridge, is similar, but it is slightly weaker and of slightly smaller dimensions than that under the Reykjanes ridge in the south. Various observations indicate the existence of plume material underlying the ridge in this area. The Kolbeinsey ridge is unusually elevated between the Tjörnes fracture zone, immediately in the north of Iceland, and Jan Mayen, approximately 1000 km further north. (Schilling 1985) proposed the existence of a plume beneath Jan Mayen. Jones *et al.* (2002) show that gravitational V-shaped ridges are visible between the Spar fracture zone (located approximately midway between Iceland and Jan Mayen, at approximately 500 km north of Iceland) and Jan Mayen. These are only apparent to the east of the ridge, probably because thick sediments from Greenland cover much of area west of the ridge. Schilling *et al.* (1999) found that the boundary on the Kolbeinsey ridge between the zone of influence of the low ^{3}He/^{4}He Jan Mayen plume and the high ^{3}He/^{4}He Iceland plume is in the vicinity of the Spar fracture zone. Taylor *et al.* (1993) show that the S_r, N_b and P_b isotope signature of the Iceland plume is as widespread as the thermal and topographic anomalies around Iceland and that the Kolbeinsey ridge is significantly affected by the Iceland plume but less so than the Reykjanes ridge to the south of Iceland. The low-velocity anomaly north of Iceland in our model could therefore result from either of two causes: the influence of the Iceland plume for approximately 500 km in the north along the Kolbeinsey ridge, or a plume under Jan Mayen.

Below 175 km depth, the low-velocity anomaly beneath Iceland decays to the PREM background level at 200–225 km depth. This decay is stronger than the apparent reduction in the anomaly amplitude with depth as a result of the frequency content and modal composition of our surface wave data (Fig. 12). This image of the low-velocity anomaly in the upper mantle beneath Iceland is of higher lateral resolution but compatible with the models of Ritsema *et al.* (1999) and Zhao (2001) at shallow (<175 km) depths. We do not resolve a narrow plume stem at deeper depths beneath Iceland as do Ritsema & Allen (2003). Allen *et al.* (1999) investigate diffraction effects of a cylindrical plume stem on the frequency dependence of shear wave arrivals measured on Iceland and conclude the plume stem must have a radius of approximately 100 km and a maximum S velocity anomaly of −12 per cent. Allen *et al.* (2002a) conclude from the analysis of a variety of seismic data that from 250–400 km beneath Iceland there exists a near-cylindrical low-velocity anomaly with a radius of 100 km and a peak S velocity anomaly of −4 per cent. Our tests (Fig. 13) show that such a structure would only be

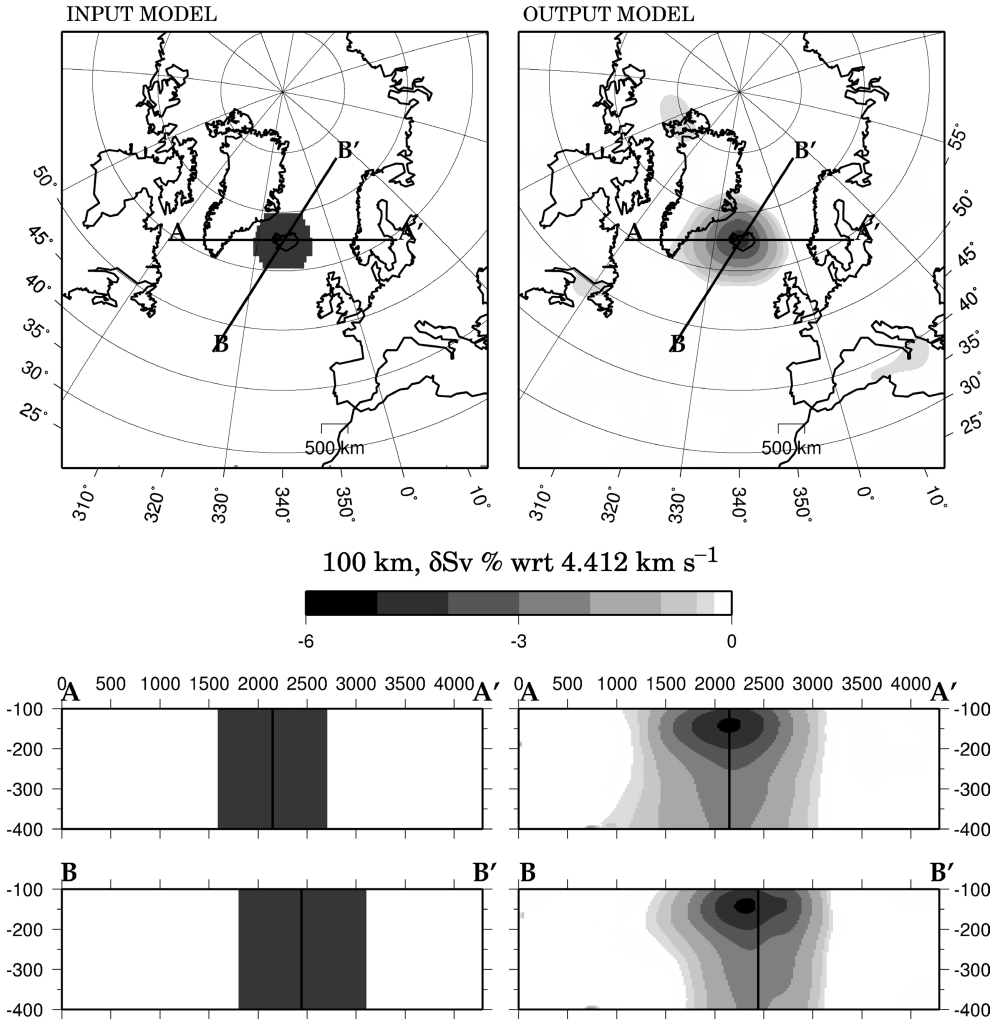

Figure 12. Synthetic seismogram experiment input (left) and output (right) models at 100 km depth and vertical sections along profiles AA′ and BB′. The input mantle model is a cylindrical low-velocity (−5 per cent with respect to PREM) anomaly, 1000 km in diameter, embedded in a smoothed PREM model. The correlation length used in the tomographic inversion was 400 km.

resolved where the higher mode content of the data is high, such as in central Europe (Fig. 8, EE′). A plume stem would not be resolved beneath the central North Atlantic ocean (Fig. 8, profiles AA′ and BB′) considering the frequency content of the data (<0.02 Hz) and lateral smoothing (400 km) used in building our tomographic model.

6.1.2 The Azores plume

The second major negative anomaly in the North Atlantic lies in an extended region beneath the Azores (Fig. 6, profiles CC′ and DD′). This anomaly, like the one associated with Iceland, is elongated along the ridge axis. At 75–150 km depth, it extends between approximately 25°–45°N, a lateral extent slightly larger than that of the Iceland plume (approximately 2200 km along-axis and 800 km perpendicular to the ridge). The Azores anomaly is both thinner vertically (75–150 km depth) and decays more rapidly with depth than the Iceland plume (compare profiles AA′ with CC′ and BB′ with DD′). These differences are also present in the global tomography results of Ritsema *et al.* (1999) shown in Montagner & Ritsema (2001). Silveira & Stutzmann (2002) used approximately 1900 dispersion measurements from regional surface waves to construct a tomographic model of the North Atlantic, extending to the Azores in the north. Although out image is of superior resolution, the general characteristics of the anomaly at depth and along the ridge are remarkably similar to the ones obtained by Silveira & Stutzmann (2002).

Even though the Azores hotspot is located 100 km east of the Mid-Atlantic ridge, long-wavelength bathymetric, gravimetric and geochemical anomalies in this region indicate plume–ridge interaction. Rare earth element concentrations (Schilling 1985) and S_r isotope ratios (Dosso *et al.* 1993; Goslin *et al.* 1998) indicate mixing of MORB and mantle plume source for 1800–1900 km along the ridge. However, the mixing is not symmetric: the ridge is geochemically affected ∼1200 km to the south but only ∼600 km to the north (Goslin *et al.* 1998) of the Azores. Gravity and bathymetry show oblique *V*-shaped ridges in the south to 27°N (Thibaud *et al.* 1997). There are no *V*-shaped ridges to the north of the hotspot and the geochemical anomaly only extends to 43°–44°N (Goslin & Triatnord Scientific Party 1999).

Ito & Lin (1995) studied the variation of the bathymetry and gravity anomalies associated with five oceanic hotspots with comparable heat fluxes, including Iceland and the Azores, with the ridge spreading rate and the hotspot—ridge-axis separation. They found

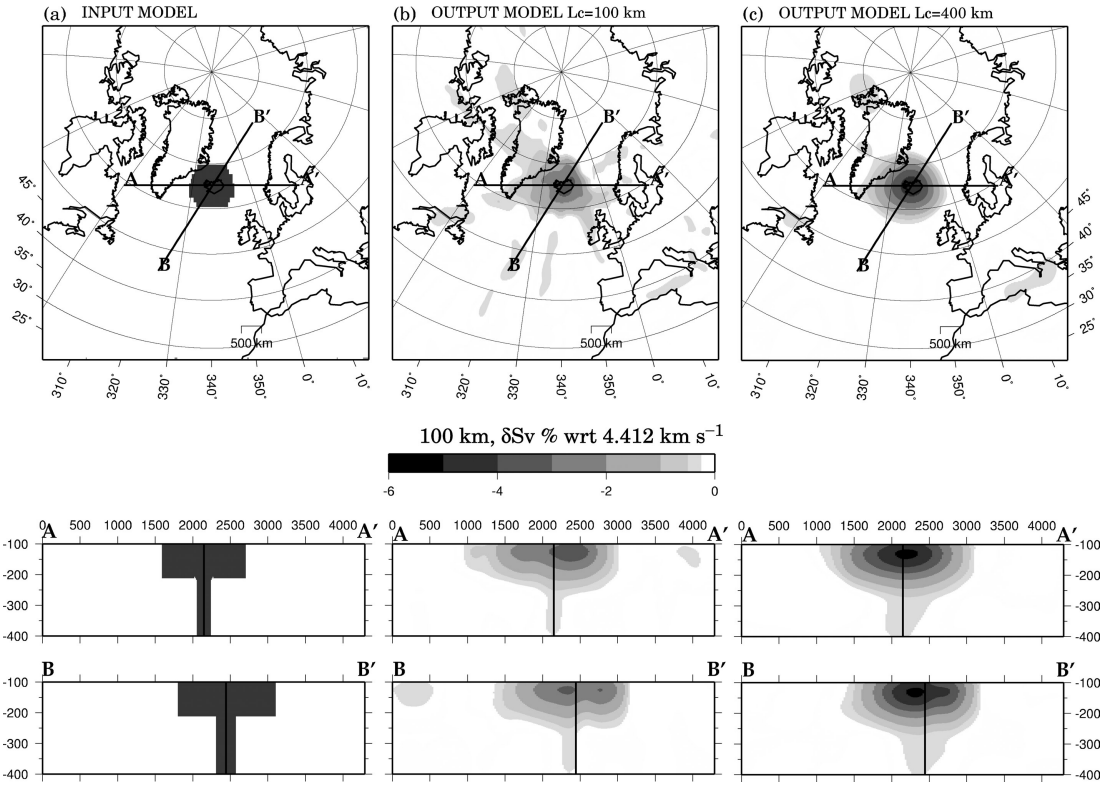

Figure 13. Synthetic experiment input (a) and output (b, c) models at 100 km depth and vertical sections along AA′ and BB′. The input mantle model is smoothed PREM with a low-velocity (−5 per cent with respect to PREM) plume-like perturbation embedded. The anomaly is centred on Iceland (65°N, 20°W) with plume head and stem diameters of 1200 and 200 km respectively and depth extents of 200 and 600 km respectively. The tomographic inversion was carried out with a correlation length of 100 (b) and 400 km (c).

that the along-axis widths of the anomalies decrease with increasing spreading rate and increasing ridge–hotspot distance and that the temperature anomaly of the plume material at the ridge axis decreases with increasing ridge–hotspot distance. The ridge spreading rates near Iceland and the Azores are 1.9 and 2.5 cm yr^{-1} respectively. Thus, Ito & Lin (1995) predict a weaker and smaller ridge anomaly for the Azores compared with Iceland, whereas we observe similar anomalies under both regions. Schilling (1991) also predicts a weaker temperature anomaly for the Azores in comparison to Iceland, implying a higher plume viscosity for the Azores plume, or a smaller viscosity contrast between the plume and the surrounding mantle than for the Iceland plume. 3-D numerical modelling experiments of Alber & Christensen (2001) show that when the viscosity contrast decreases, the plume head tends to be shallower, consistent with our observations, but becomes less elongated along the ridge axis, inconsistent with our tomographic results. However, the ridge spreads obliquely in the Azores area, which could cause an increase of the along-axis width of the anomaly, resulting in a similar lateral extent of the Iceland and Azores plume heads.

6.1.3 The Eifel plume

The Eifel volcanic field, located in the Rhenish massif, northwest Germany, is the product of approximately 300 small eruptions, which occurred between 10 800 and 700 000 yr ago. Although the total volume of volcanic products is small (smaller than 15 km^3), ongoing mantle helium outgassing (Griesshaber *et al.* 1992) and isotopic and trace element signatures (Hoernle *et al.* 1995) support a plume origin for these volcanics. Keyser *et al.* (2002) inverted approximately 5000 traveltimes of *S* waves recorded on a large seismic network across the Eifel volcanic field and find a low-velocity zone, approximately 100 km in diameter, extending to at least 400 km depth. The *S*-wave velocity contrast is depth-dependent and varies from −5 per cent at 31 to 100 km depth to at least −1 per cent at 400 km depth. This low-velocity feature is not continuous, but there is a gap between approximately 170 and 240 km depth where the anomaly nearly disappears. Keyser *et al.* (2002) suggest that the observed low velocities are consistent with a plume beneath the Eifel volcanic field with an excess temperature of 200–300 °C, similar to Iceland, and that the gap in the *S*-wave velocity structure may result from an increase of the shear modulus caused by dehydration.

There is a strong low-velocity anomaly in our model (Fig. 5) beneath western Europe. This anomaly is present in the inversion results irrespective of our choice of crustal model and is therefore not likely to be an artefact of our choice of fixed crustal model unless both crustal models are significantly wrong in the same way in this area. The path density and azimuthal coverage are excellent for this region (Fig. 2). As a result of the greater higher mode path density in central Europe, the *a posteriori* error is lowest at depth in this part of the model (Fig. 7). The resolution tests (Figs. 10 and 11) indicate that this is in the best resolved region of our model. At 75 km depth, a strong low-velocity anomaly occurs beneath southeastern Great Britain. A strong negative anomaly occurs in the same geographical location at 80 km depth in the model of Marquering & Snieder (1996). With increasing depth, this low-velocity feature shifts to the east to approximately below the location of the Eifel hotspot. At depths greater than 150 km, the location of this feature remains

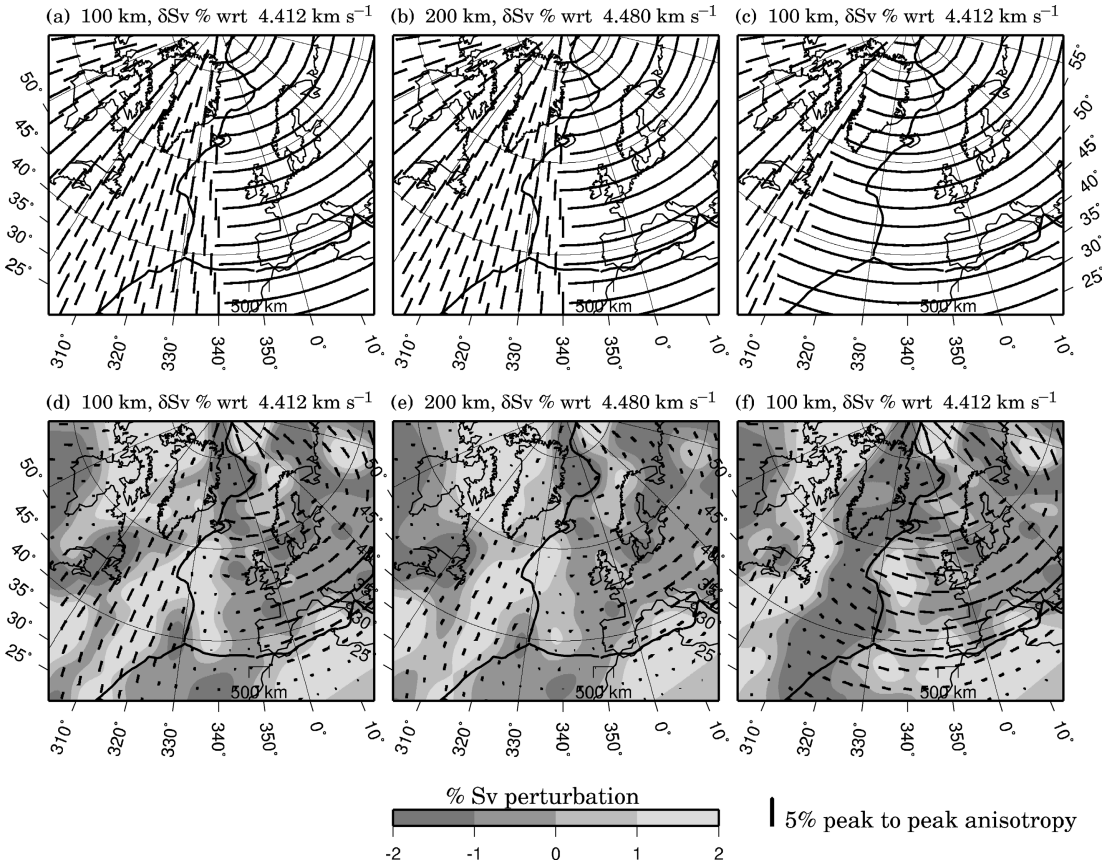

Figure 14. Synthetic seismogram experiment for azimuthal anisotropy. Horizontal sections through the input (a, b, c) and output models (d, e, f). The input model is smoothed PREM with added 5 per cent peak-to-peak azimuthal anisotropy. The directions of fast horizontally propagating S_v waves are shown by the black bars, the length of which is proportional to the peak-to-peak azimuthal anisotropy. The input models (a) and (c) are the same except that the anisotropy pattern is rotated by 45° anticlockwise.

constant but the amplitude decreases with depth, approximately as in the test results shown in Fig. 12, suggesting that the structure has a low-velocity perturbation with respect to PREM of 4–5 per cent down to 400 km depth.

The low-velocity structure in our model beneath the same region is remarkably similar to a smoothed image of the *S*-wave structure seen by Keyser *et al.* (2002). At shallow depth (75–100 km), the shear wave velocity in our model is 7–8 per cent slow with respect to PREM. The anomaly weakens with depth and becomes −3 per cent slow with respect to PREM at 275 to 325 km depth. There is a zone between 175 and 225 km depth where the anomaly is weak. However, preliminary results from a tomographic inversion using a data set consisting of approximately 9000 waveforms (unpublished work) show that the amplitude distribution between 125–400 km is much simpler; the amplitude decays with depth in a manner that is remarkably similar to the recovered model of the cylinder resolution test, suggesting that the structure actually remains approximately 4–5 per cent slow with respect to PREM between 50–400 km depth.

If the 1000-km-wide low-velocity zone at shallow (75–100 km) depth is in fact the head of the Eifel plume, the structure is significantly smaller than that of the Icelandic plume despite the excess temperatures of the two plumes being similar as proposed by Keyser *et al.* (2002). Both the smaller head of the Eifel plume and the smaller total erupted volume of volcanic material may result from a smaller total heat flux plume trapped beneath a thicker continental plate. In this case, the degree of decompression melting in the Eifel plume would be small compared with the degree of decompression melting for the higher heat flux Icelandic plume beneath the thin oceanic plate.

6.2 Azimuthal anisotropy

The azimuthal anisotropy results (Fig. 5) show a large amplitude (up to 6 per cent) and complex pattern of azimuthal anisotropy in the shallow (75–150 km depth) layers. While the general pattern is similar at all depths, the amplitude decays with depth. In the parts of the model deeper than 200 km, the amplitude is reduced to ∼1 per cent in oceanic areas and to ∼2 per cent in western Europe. The resolution tests have shown that the anisotropy pattern is a robust feature of the model in most areas of the model, including the ocean, the area around Iceland and west Europe, and throughout the depth range of 50–400 km, but the recovered amplitude is underestimated, especially at depths exceeding 175 km. Therefore, the observed decay of amplitude with depth can be partly caused by resolution loss. At 100–200 km depth, the amplitude of the azimuthal anisotropy is larger in the European Plate than it is in the North American Plate, but this difference also decreases with increasing depth.

In the oceanic region south of approximately 50°N, the fast direction of horizontally propagating S_v waves is perpendicular to the ridge axis and approximately in the spreading direction of the ridge. This is coherent throughout the depth range of the model. Fast-spreading mid-ocean ridge environments are associated with large mantle deformation stresses and the mantle flow pattern is

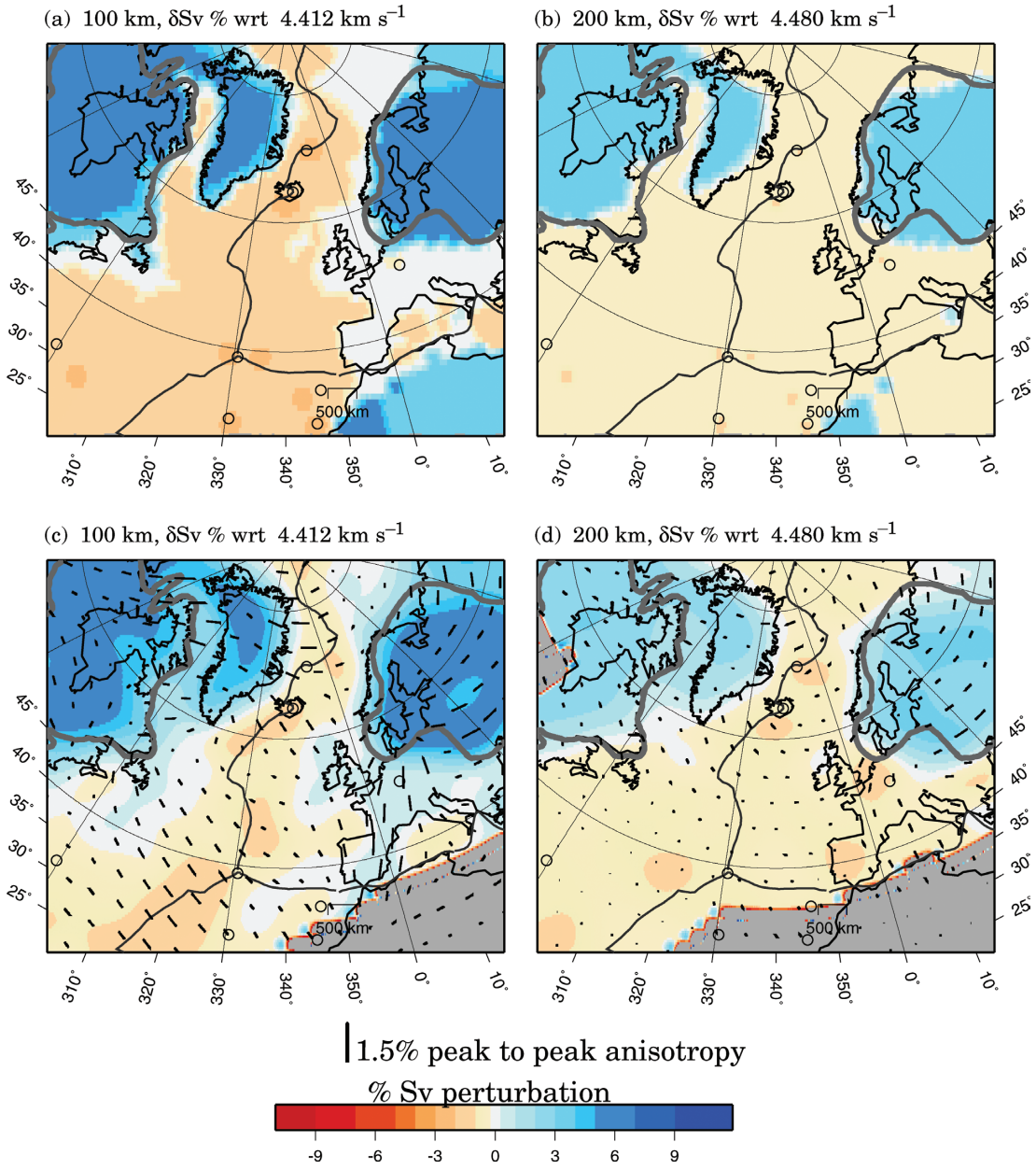

Figure 15. Synthetic seismogram experiment for the trade-off between heterogeneity and anisotropy. Horizontal sections through the input (a,b) and output models (c,d) at 100 and 200 km depth. The input model is the 3SMAC isotropic mantle model. In (c) and (d), the directions of fast horizontally propagating S_v waves are shown by the black bars, the length of which is proportional to the peak-to-peak azimuthal anisotropy.

expected to be directly mapped in azimuthal anisotropy: the direction of fast S_v-wave propagation is expected to be along the horizontal projection of the fast (α) axis of olivine (Nicolas & Christensen 1987).

In the area of the Iceland plume head, north of 50°N, the pattern abruptly changes from having an E–W fast axis to having a NNW–SSE fast axis. As Li & Detrick (2003) point out, the mantle flow beneath Iceland is affected by three main processes: (i) a possibly radial flow of plume material in the plume head, (ii) NWW–SEE flow as a result of the spreading ridge and (iii) NE–SW channelled flow of plume material beneath the ridge. The resultant mantle flow must be a combination of these three main processes, depending on the relative flow speeds. However, the recent study of Kaminski & Ribe (2002) shows that seismic anisotropy and mantle flow are not simply related in such a complex environment. The authors demonstrate that in a ridge-plume environment the lattice-preferred orientation (LPO) of olivine is strongly perturbed in the vicinity of the hotspot in an area five times wider than the radius of the plume stem, but there is no consistency between the LPO and mantle flow. We are therefore currently unable to make conclusive statements for the mantle flow in the vicinity of Iceland.

Shear wave splitting measurements at a number of stations across Iceland also give a consistent NW–SE fast polarization direction (Bjarnason *et al.* 1996, 2002; Li & Detrick 2003), except in the area near the west coast, where the average direction is N–S. The anisotropy resulting from shear wave splitting measurements represents the depth-averaged anisotropic structure directly beneath the stations. On the other hand, surface waves are affected by a much

wider lateral area and therefore give the long-wavelength anisotropy, but with good vertical resolution. Anisotropy constraints from body and surface waves do not arise from sampling precisely the same structure and should should not be directly compared. However, in this case the body wave results are horizontally coherent over several hundred kilometres, indicating that the anisotropy pattern is similar over a wide area around Iceland. This is confirmed by the surface wave anisotropy results of this study. The results also show that the fast direction remains constant throughout the depth range of the model (50–400 km), which is in agreement with the shear wave splitting results.

Li & Detrick (2003) examined the phase velocities of Rayleigh waves recorded at stations across Iceland and constructed 2-D phase velocity maps for different periods in the range of 25–67 s. They found that for surface waves in the period range of 50–67 s, which are mostly affected by the Earth structure between approximately 50–100 km depth, the fast directions are in the NW–SE direction in central and east Iceland, again in agreement with the results presented here. Global tomography models also give similar fast propagation directions in the area surrounding Iceland. For example, the global phase velocity model of Ekström (2001) shows that the fast propagation direction of Rayleigh waves of periods of 50–150 s changes from NWW–SEE in the ocean south of Iceland to NW–SE in the area around Iceland.

The fast axis in NW Europe, near the location of the Eifel plume, is at all depths in the NW–SE direction. Near the low-velocity anomaly beneath the Iberian peninsula, the amplitude of anisotropy at 100 km depth is almost reduced to zero. The latter could be associated with the proposed convective mantle upwelling, which causes the high elevation of the Iberian peninsula (McKenzie, private communication, 2003).

The resolution experiments have shown that the anisotropy pattern is not properly recovered in regions where abrupt changes in the fast direction occur over distances much smaller than a wavelength. Such small-scale anisotropy variations are common in the lithosphere and the interpretation of anisotropy in these parts of the model is therefore risky.

7 CONCLUSIONS

In this paper, we present a 3-D S_v-wave velocity and azimuthal anisotropy model for the upper mantle beneath the North Atlantic and surrounding regions derived from the analysis of over 3000 multimode Rayleigh wave seismograms. The dense path coverage, the wide azimuthal distribution and the substantial higher mode content of the data set as well as the short path-lengths in the data set have enabled us to build an upper-mantle model for the region with a horizontal resolution of a few hundred kilometres extending to 400 km depth. The extensive testing we carried out demonstrates that we achieve good resolution both laterally, as a result of dense ray coverage and good azimuthal coverage, and vertically, as a result of multimode analysis and a wide frequency range. However, because of the uneven distribution of higher modes, depth resolution is better in central Europe than in the central North Atlantic ocean.

Well-known features, such as continental cratons (Canadian, Greenland, East European) and the Tornquist–Teisseyre zone are very clearly imaged. Low-velocity anomalies are present in the upper-mantle model beneath each of the Iceland, the Azores and Eifel hotspots. The observed low-velocity anomalies beneath the Iceland and Azores hotspots are approximately 4–7 per cent slow with respect to PREM, they are confined in the top 200 km of the mantle and they are significantly elongated along the Mid-Atlantic ridge. In contrast, the Eifel anomaly extends to at least 400 km depth, it is not elongated in any preferred direction and the anomaly strength does not decrease monotonically with depth, but has a higher velocity zone at approximately 200 km depth, which is in agreement with a previous study.

The elongation of the anomalies beneath the two near-ridge-centred hotspots of Iceland and the Azores is indicative of a strong plume–ridge interaction resulting in channelling and flow of the plume mantle material beneath the ridge. This is in agreement with geochemical studies and several geophysical observations in both of these areas and numerical experiments modelling mantle buoyancy-upwelling beneath ridge-like structures. We found no low-velocity features that might be interpreted as plume stems beneath the two oceanic hotspots. However, synthetic seismogram experiments show that a narrow plume tail is at the limit of resolution of our surface wave data set. The resolution of a plume tail requires the combination of body wave and surface wave constraints (e.g. Ritsema *et al.* 1999). Compared with the anomaly associated with Iceland, the Azores anomaly is elongated further along the ridge, probably as a result of the oblique ridge-spreading in the area of the Azores. The Azores anomaly is also thinner and decays more rapidly with depth than the Icelandic anomaly, implying a lower viscosity contrast between the plume and and surrounding mantle material.

The fast propagation direction of horizontally propagating S_v waves is consistent throughout the depth range of the model (50–400 km) beneath the ocean. In the ocean south of Iceland, the fast direction correlates well with the E–W plate motion and the ridge-spreading direction. This is more pronounced in the part of the ocean to the east of the ridge. The consistency between the plate motion direction and the fast propagation direction shows that the plate motion dominates the upper-mantle flow beneath the North Atlantic and governs the LPO of olivine over large scales, giving rise to the observed long-wavelength anisotropy pattern. This is an expected characteristic of olivine-rich aggregates deformed by large progressive simple shear. In a large area surrounding Iceland, this simple pattern is disrupted and the fast propagation direction changes to NW–SE. Shear wave splitting studies as well as local and global phase velocity tomography studies find a similar fast propagation direction beneath most areas of Iceland. A recent theoretical study shows that the simple relation that exists between LPO and mantle flow beneath a fast spreading ridge is lost when an additional flow type (rising plume) is introduced. Seismic anisotropy and mantle flow are therefore not simply related in a complex environment such as the upper mantle beneath the area of Iceland and so no conclusive statements can be currently made.

ACKNOWLEDGMENTS

We would like to thank the people who helped with the NEAT station operation (J. McKenzie, C. Lightfoot, K. Raven, J. Parke, A. Brisbourne, J. Ásgeirsson, H. Brynjólfsson, T. Rasmussen) and the people who provided access to their land for sites (Glenveigh National Park staff, B. Watters, B. Bjarnason). The instruments for the stations we deployed were supplied by SEIS-UK. We obtained seismic data through the IRIS data center from the IRIS-IDA, IRIS-USGS, SRO/ASRO, Geoscope, Geofon, Mednet and Czech Regional Seismic Networks and from the HOTSPOT and ICEMELT temporary networks on Iceland. We also obtained data from the University of Uppsala network in Sweden, the Canadian National Seismological Data Centre, AWE Blacknest Seismology group, the Norwegia

Institute of Solid Earth Physics, Iceland Meterological Office, and the Danish National Survey, Cadastre group and KMS. This work has profited from numerous discussions with D. McKenzie. SP would like to acknowledge PhD studentship support from the A.G. Leventis Foundation, the Danish Lithosphere Center and the Cambridge Commonwealth/Overseas Trust. All maps were created with the generic mapping tools (gmt) data and display package.

REFERENCES

Alber, M. & Christensen, U., 2001. Channeling of plume flow beneath mid-ocean ridges, *Earth planet. Sci. Lett.,* **187,** 207–220.

Allen, R. *et al.*, 1999. The thin hot plume beneath Iceland, *Geophys. J. Int.,* **137,** 51–63.

Allen, R. *et al.*, 2002a. Imaging the mantle beneath Iceland using integrated seismological techniques, *J. geophys. Res.,* **107**(B12), 10.1019/2001JB000595.

Allen, R. *et al.*, 2002b. Plume driven plumbing and crustal formation in Iceland, *J. geophys. Res.,* **107**(B8), 0.1029/2001JB000584.

Alsina, D. & Snieder, R., 1996. Constraints on the velocity strucutre beneath the Tornquist-Teisseyre zone from beamforming analysis, *Geophys. J. Int.,* **126**(1), 205–218.

Bassin, C., Laske, G. & Masters, G., 2000. The current limits of resolution for surface wave tomography in North America, *EOS, Trans. Am. geophys. Un.,* **81,** 897.

Bijwaard, H. & Spakman, W., 1999. Tomographic evidence for a narrow whole mantle plume below Iceland, *Earth planet. Sci. Lett.,* **166,** 121–126.

Bjarnason, I., Menke, W., Flóvenz, O. & Caress, D., 1993. Tomographic image of the spreading center in southern Iceland, *J. geophys. Res.,* **98,** 6607–6622.

Bjarnason, I., Wolfe, C. & Solomon, S., 1996. Initial results from the ICEMELT experiment: Body-wave delay times and shear-wave splitting across Iceland, *J. geophys. Res.,* **23**(5), 459–462.

Bjarnason, I., Silver, P., Rümpker, G. & Solomon, S., 2002. Shear wave splitting across the Iceland hotspot: Results from the ICEMELT experiment, *J. geophys. Res.,* **107**(B12), 2382.

Cara, M. & Lévêque, J., 1987. Waveform inversion using secondary observables, *Geophys. Res. Lett.,* **14,** 1046–1049.

Cotte, N., Pedersen, H., Campillo, M., Farra, v. & Cansi, Y., 2000. Off-great-circle propagation of intermendiate period surface waves observed on a dense array in the French Alps, *Geophys. J. Int.,* **142,** 825–840.

Dahl-Jensen, T. *et al.*, 2003. Depth to Moho in Greenland: Receiver Function Analyses suggest two Proterozoic Blocks in Greenland, *Earth planet. Sci. Lett.,* **205**(3–4), 379–393.

Darbyshire, F., Priestley, K., White, R., Stefánsson, R., Gudmundsson, G. & Jakobsdóttir, S., 2000a. Crustal structure of central and northern Ireland from analysis of teleseismic receiver functions, *Geophys. J. Int.,* **143**(1), 163–184.

Darbyshire, F., White, R. & Priestley, K., 2000b. Structure of the crust and uppermost mantle of Iceland from a combined seismic and gravity study, *Earth planet. Sci. Lett.,* **181**(3), 409–428.

Debayle, E., 1999. Sv-wave azimuthal anisotropy in the Australian upper mantle: preliminary results from automated Rayleigh waveform inversion, *Geophys. J. Int.,* **137,** 747–754.

Debayle, E. & Kennett, B., 2000. Anisotropy in the Australasian upper mantle from Love and Rayleigh waveform inversion, *Earth planet. Sci. Lett.,* **184,** 339–351.

Debayle, E. & Kennett, B., 2003. Surface-wave studies in the Australian region, *Geological Society of Australia Special Publications,* **22,** 19–34.

Debayle, E. & Sambridge, M., 2004. Inversion of massive surface wave data sets: Model construction and resolution assessment, *J. geophys. Res.,* **109**(B2), 10.1029/2003JB002652.

Debayle, E., J.-J., Lévêque & Cara, M., 2001. Seismic evidence for a plume in the upper mantle beneath the northeastern Afro/Arabian continent, *Earth planet. Sci. Lett.,* **193,** 423–436.

Dosso, L., Bougault, H. & Joron, J.-L., 1993. Geochemical morphology of the North Mid-Atlantic Ridge, 10° –24°N: trace element-isotope complementary, *Earth planet. Sci. Lett.,* **120,** 443–462.

Dziewonski, A. M. & Anderson, D., 1981. Preliminary Reference Earth Model, *Phys. Earth planet. Int.,* **25**(4), 297–356.

Ekström, G., 2001. Mapping azimuthal anisotropy of intermediate-period surface waves (abstract), *EOS, Trans. Am. geophys. Un.,* **82**(47), S51E–06.

Faccenna, C., Jolivet, L., Piromallo, C. & Morelli, A., 2003. Subduction and the depth of convection in the Mediterranean mantle, *J. geophys. Res.,* **108,** ETG9–1/13.

Fitton, J., Saunders, A., Norry, M., Hardarson, B. & Taylor, R., 1997. Thermal and chemical structure of the Iceland plume, *Earth planet. Sci. Lett.,* **153,** 197–208.

Foulger, G. *et al.*, 2001. Seismic tomography shows that upwelling beneath Iceland is confined to the upper mantle, *Geophys. J. Int.,* **146,** 504–530.

Gaherty, J., 2001. Seismic evidence for hotspot-induced buoyant flow beneath the Reykjanes Ridge, *Science,* **293,** 1645–1647.

Goslin, J. & Triatnord Scientific Party, 1999. Extent of azores plume influence on the Mid-Atlantic Ridge north of the hotspot, *Geophys. J. Int.,* **27**(11), 991–994.

Goslin, J., Thirot, J.-L., Noel, O. & Francheteau, J., 1998. Slow-ridge/hotspot interactions from global gravity, seismic tomography and $^{87}Sr/^{86}Sr$ isotope data, *Geophys. J. Int.,* **135,** 700–710.

Griesshaber, E., O'Nions, R. & Oxburgh, E., 1992. Helium abd carbon isotope systematics in crustal fluids from the Eifel, the Rhine Graben and the Black Forest, FRG, *Chem. Geol.,* **99,** 213–235.

Gudmundsson, O., 2003. The dense root of the Iceland crust, *Earth planet. Sci. Lett.,* **206,** 427–440.

Helmberger, D., Wen, L. & Ding, X., 1998. Nature of the crust mantle transition zone and the thermal state of the upper mantle beneath Iceland from gravity modelling, *Nature,* **3967,** 251–255.

Hoernle, K., Zhang, Y.-S. & Graham, D., 1995. Seismic and geochemical evidence for large-scale mantle upwelling beneath the eastern Atlantic and western and central Europe, *Nature,* **374,** 34–39.

Ito, G. & Lin, J., 1995. Oceanic spreading center-hotspot interactions: Constraints from along-isochron bathymetric and gravity anomalies, *Geology,* **23,** 657–660.

Jones, S., White, N. & Maclennan, J., 2002. V-shaped ridges around Iceland:implications for spatial and temporal patterns of mantle convection, *Geochem. Geophys. Geosyst.,* **3**(10), 1059, 2002GC000361.

Kaban, M., Flóvenz, O. & Pálmason, G., 2002. Nature of the crust mantle transition zone and the thermal state of the upper mantle beneath Iceland from gravity modelling, *Geophys. J. Int.,* **149,** 281–299.

Kaminski, E. & Ribe, N., 2002. Timescales for the evolution of seismic anisotropy in mantle flow, *Geochem. Geophys. Geosyst.,* **3**(8), pp 1–17.

Keller, W., Anderson, D. & Clayton, R., 2000. Resolution of tomographic models of the mantle beneath Iceland, *Geophys. Res. Lett.,* **27,** 3993–3996.

Kennett, B., 1995. Approximations for surface–wave propagation in laterally varying media, *Geophys. J. Int.,* **122,** 470–478.

Keyser, M., Ritter, J. & Jordan, M., 2002. 3D shear-wave velocity structure of the Eifel plume, Germany, *Earth planet. Sci. Lett.,* **203,** 59–82.

Lévêque, J.-J., Cara, M. & Rouland, D., 1991. Waveform inversion of surface wave data: test of a new tool for systematic investigation of upper mantle structure, *Geophys. J. Int.,* **104,** 565–518.

Lévêque, J.-J., Rivera, L. & Wittlinger, G., 1993. On the use of the checkerboard test to assess the resolution of tomographic inersions, *Geophys. J. Int.,* **115,** 313–318.

Lévêque, J.-J., Debayle, E. & Maupin, V., 1998. Anisotropy in the Indian Ocean upper mantle from Rayleigh and Love waveform inversion, *Geophys. J. Int.,* **133,** 529–540.

Li, A. & Detrick, R., 2003. Azimuthal anisotropy and phase velocity beneath iceland: implication for plume-ridge interaction, *Earth planet. Sci. Lett.,* **6763,** 1–13.

McKenzie, D., 1984. Generation and compaction of partial molten rock, *J. Petrol.,* **25,** 713–765.

Maggi, A. & Priestley, K., 2003. Surface waveform tomography of the Iranain and Anatolian Plateaus, *Geophys. J. Int.*, submitted.

Marquering, H. & Snieder, R., 1996. Shear-wave velocity structure beneath Europe, the northeastern Atlantic and western Asia from waveform inversion including surface-wave mode coupling, *Geophys. J. Int.,* **127,** 283–304.

Marquering, H., Snieder, R. & Nolet, G., 1996. Waveform inversion and the significance of surface-wave mode coupling, *Geophys. J. Int.,* **124,** 258–278.

Montagner, J., 1986. Regional three-dimensional structures using long-period surface waves, *Ann. Geophys.,* **4,** 283–294.

Montagner, J. & Ritsema, J., 2001. Interactions between Ridges and plumes, *Science,* **294,** 1472–1473.

Nataf, H.-C. & Ricard, Y., 1996. 3SMAC: an *a priori* tomographic model of the upper mantle based on geophysical modeling, *Phys. Earth planet. Int.,* **95,** 101–122.

Nicolas, A. & Christensen, N., 1987. Formation of anisotropy in the upper mantle peridotides: A review, in, *Composition, Structure and Dynamics of the Lithosphere/Asthenosphere System*, pp. 111–123, eds Fuchs, K. & Froidevaux, C., Am. Geophys. Un., Washington, DC.

Nishimura, C. & Forsyth, D., 1989. The anisotropic structure of the upper mantle in the Pacific, *Geophys. J. Int.,* **96,** 203–229.

Nolet, G., 1990. Partitioned waveform inversion and two-dimensional structure under the Network of Autonomously Recording Seismographs, *J. geophys. Res.,* **95,** 8499–8512.

Pilidou, S., 2004. Upper Mantle Shear-wave Velocity and Anisotropy Structure beneath the North-Atlantic: A seismic image of the Iceland mantle plume, *PhD thesis*, Cambridge University, Cambridge.

Priestley, K. & Debayle, E., 2003. Seismic evidence for a moderately thick lithosphere beneath the Siberian Platform, *Geophys. Res. Lett.,* **30**(3), 10.1029/2002GL015931.

Priestley, K. & Tilmann, F., 1999. Shear-wave structure of the lithosphere above the Hawaiian hotspot from two–station Rayleigh wave phase velocity measurements, *Geophys. Res. Lett.,* **26,** 1493–1496.

Ritsema, J. & Allen, R., 2003. The elusive mantle plume, *Earth planet. Sci. Lett.,* **207,** 1–12.

Ritsema, J., van Heijst, H. & Woodhouse, J., 1999. Complex shear wave velocity structure imaged beneath Africa and Iceland, *Science,* **286,** 1925–1928.

Ritzwoller, M. & Levshin, A., 1998. Eurasian surface wave tomography: Group velocities, *J. geophys. Res.,* **103,** 4839–4878.

Ritzwoller, M., Shapiro, N., Barmin, M. & Levshin, A., 2002. Global surface wave diffraction tomography, *J. geophys. Res.,* **107**(B12), 10.1029/2002JB001777.

Schilling, J., 1973. Iceland mantle plume: geochemical study of Reykjanes Ridge, *Nature,* **242,** 65–571.

Schilling, J., 1985. Upper mantle heterogeneities and dynamics, *Nature,* **314,** 65–67.

Schilling, J., 1991. Fluxes and excess temperatures of mantle plumes inferred from their interaction with migrating mid-ocean ridges, *Nature,* **352,** 397–403.

Schilling, J., Kingsley, R., Fontignie, D., Poreda, R. & Xue, S., 1999. Dispersion of the Jan Mayen and Iceland mantle plumes in the arctic: A He-Pb-Nd-Sr isotope tracer study of basalts from the Kolbeinsey, Mohns and Knipovich Ridges, *J. geophys. Res.,* **104**(5), 10 543–10 569.

Searle, R., Keeton, J., Owens, R., White, R., Mecklenburgh, R., Parsons, B. & Lee, S., 1998. The Reykjanes Ridge: structure and tectonics of a hot-spot-influenced, slow-spreading ridge, from multibeam bathymetry, gravity and magnetic investigations, *Earth planet. Sci. Lett.,* **160,** 463–478.

Shen, Y., S.C., S., Bjarnason, I. & Purdy, G., 1996. Hot mantle transition zone beneath Iceland and the adjacent Mid-Atlantic Ridge inferred from P-to-S conversions at the 410- and 660-km discontinuities, *Geophy. Res. Lett.,* **23,** 3527–3530.

Shen, Y., S.C., S., Bjarnason, I. & Wolfe, C., 1998. Seismic evidence for a lower mantle origin of the Iceland mantle plume, *Nature,* **395,** 62–65.

Silveira, G. & Stutzmann, E., 2002. Anisotropic tomography of the Atlantic Ocean, *Phys. Earth planet. Int.,* **132,** 237–248.

Sleep, N., 1990. Hotspots and mantle plumes: Some phenomenology, *J. geophys. Res.,* **95,** 6715–6736.

Sleep, N., 1996. Lateral flow of hot plume material ponded at sublithospheric depths, *J. geophys. Res.,* **101**(B12), 28 065–28 083.

Smallwood, R. & White, R., 1998. Crustal accretion at the Reykjanes Ridge, 61°–62°N, *J. geophys. Res.,* **103,** 5185–5201.

Spetzler, J., Trampert, J. & Snieder, R., 2002. The effect of scattering in surface wave tomography, *Geophys. J. Int.,* **149,** 755–767.

Staples, R., White, R., Brandsdóttir, B., Menke, W., Maguire, P., McBride, J. & Smallwood, J., 1997. Faeroe-Iceland Ridge Experiment—I. The crustal structure of north-eastern Iceland, *J. geophys. Res.,* **102,** 7849–7866.

Tarantola, A. & Valette, B., 1982. Generalized nonlinear inverse problems solved using the least squares criterion, *Rev. Geophys. Space Phys.,* **20,** 219–232.

Taylor, R., Thirlwall, M., Murton, B., Hilton, D. & Gee, M., 1993. Isotopic constraints on the influence of the Icelandic plume, *Earth planet. Sci. Lett.,* **148,** E1–E8.

Thibaud, R., Gente, P. & Maia, M., 1997. A systematic analysis of the Mid-Atlantic Ridge morphology and gravity between 15°N and 40°N, *J. geophys. Res.,* **103**(B10), 24 223–24 243.

Tryggvason, E., Husebye, E. & Stefánsson, R., 1983. Seismic image of the hypothesized Icelandic hotspot, *Tectonophysics,* **100,** 97–118.

Vogt, P., 1971. Asthenosphere motion recorded by the ocean floor south of Iceland, *Earth planet. Sci. Lett.,* **13,** 153–160.

Watson, S. & McKenzie, D., 1991. Melt generation by plumes: A study of hawaiian volcanism, *J. Petrol.,* **32,** 501–537.

White, R., McKenzie, D. & O'Nions, R., 1992. Oceanic crustal thickness from seismic measurements and rare earth element inversions, *J. geophys. Res.,* **97,** 683–715.

Wolfe, C., Bjarnason, I., VanDecar, J. & Solomon, S., 1997. Seismic study of the Iceland mantle plume, *Nature,* **385,** 245–247.

Woodhouse, J., 1974. Surface waves in a laterally varying layered structure, *Geophys. J. R. astr. Soc.,* **37,** 461–490.

Yoshizawa, K. & Kennett, B., 2002. Determination of the influence zone for surface wave paths, *Geophys. J. Int.,* **149,** 440–453.

Zhang, Y. & Lay, T., 1999. Evolution of oceanic upper mantle, *Phys. Earth planet. Int.,* **114,** 71–80.

Zhao, D., 2001. Seismic structure and origin of hotspots and mantle plumes, *Earth planet. Sci. Lett.,* **192,** 251–265.

Zielhuis, A. & Nolet, G., 1994. Shear wave velocity variations in the upper mantle beneath central Europe, *Geophys. J. Int.,* **117,** 695–715.